Study and characterization of the ZnPc:C_{60}/MoO_x interface in organic solar cells by means of photoelectron spectroscopy

Caterina Stenta

April, 2013

Dissertation to obtain the academic degree of

Master in materials engineering

submitted to the

Faculty of science and engineering of Universidade Nova de Lisboa

prepared at the

Helmholtz-Zentrum Berlin für Materialien und Energie

Supervisor: Prof. Dr. João Pedro Veiga

Co-supervisor: Dr. Iver Lauermann

Study and characterization of the ZnPc:C_{60}/MoO_x interface in organic solar cells by means of photoelectron spectroscopy

For my family

"Life is and will ever remain an equation incapable

of solution, but it contains certain known factors."

Nikola Tesla

Contents

Acknowledgments

I would like to thank Prof. Dr. Martha Ch. Lux-Steiner for giving me the opportunity to work on my thesis in her department at Helmholtz Zentrum Berlin.

Special thanks go to Dr. Iver Lauermann for letting me realize this work in his group, for his scientific supervision, guidance and for the proof-reading of this work.

I am very thankful to the CISSY group, Dr. Iver Lauermann, Alexander Steigert, Britta Höpfner and Lisa Risch for the discussions in the interpretation of XPS and UPS results, for helping me during my experience at the Helmholtz Zentrum Berlin and for the overall support.

I am very thankful to Dr. Marin Rusu for the support and guidance during the IVT measurements and for the fruitful discussions, and to Sven Wiesner, Volker Hinrichs and Tayfun Mete for helping me with the interpretation of the IVT results and for the support during the experimental work in Wannsee.

I would like to thank Prof. João Paulo Borges for the technical support and João Pedro Veiga for the guidance, the enthusiasm and the dissertation corrections.

List of symbols and abbreviations

A	Diode quality factor
AFM	Atomic force microscope
AM1.5G	Air Mass 1.5 Global
a.u.	Arbitrary units
α	Absorption coefficient
BE	Binding energy
EC	Conduction band minimum
E_F	Fermi level
E_g	Band gap energy
E_k	Kinetic energy
EQE	External quantum efficiency
ESCA	Electron spectroscopy for chemical analysis
EV	Valence band maximum
NEXAFS	Near edge X-ray absorption fine structure
ε_r	Relative dielectric constant
FF	Fill factor
φ	Work function
φ_s	Spectrometer work function
η	Energy conversion efficiency
h	Planck's constant
HOMO	Highest occupied molecular orbit
I	Current

I_{ilu}	Illumination intensity
I_0	Initial light intensity
I_{sc}	Short circuit current
ITO	Indium tin oxide
J	Current density
J_0	Saturation current density
J_m	Current density at maximum power point
J_{sc}	Short circuit current density
LUMO	Lowest unoccupied molecular orbit
k	Boltzmann constant
KPFM	Kelvin probe force microscope
μ	Charge mobility
n	Excitonic diffusion length
η	Efficiency
OVPD	Organic vapour phase deposition
OPV	Organic photovoltaic
OSC	Organic solar cell
PCE	Power conversion efficiency
PES	Photoelectron spectroscopy
P_{in}	Power of the incident light
P_{max}	Maximum power
PV	Photovoltaic
R2R	Roll to roll machinery

q	Elementary electric charge
R_lLoad	Resistor
R_s	Series resistance
R_{sh}Shunt	resistance
λ	Inelastic mean free path or wavelenght
ν	Frequency
R	Reflectance
SECO	Secondary electron cutoff
SEM	Scanning electron microscope
t	Thickness
T	Transmission or Temperature
UHV	Ultra high vacuum
UPS	Ultraviolet photoelectron spectroscopy
UV	Ultraviolet
VB	Valence band
Vis	Visible
V_{oc}	Open circuit voltage
V_m	Voltage at maximum power point
VPD	Vapour phase deposition
VTE	Vacuum thermal evaporation
Wf	Workfunction
XES	X-ray emission spectroscopy
XPS	X-ray photoelectron spectroscopy
$\square$	Square

List of figures

List of tables

Resumo

A procura de sistemas fotovoltaicos de baixo custo tem levado à escolha de materiais orgânicos como possíveis candidatos para substituir os dispositivos baseados em silício. Os materiais orgânicos têm coeficientes de absorção elevados, permitindo o uso de películas muito finas e de técnicas de fabricação de baixo custo. O controlo sobre a estrutura electrónica das interfaces orgânicas/inorgânicas em semicondutores é um passo essencial para o desenvolvimento desses dispositivos. No presente estudo esta questão é abordada numa célula solar orgânica com uma estrutura invertida, constituída por uma camada fotoactiva orgânica de zinco ftalocianina dopada com Fulereno, um eléctrodo de óxido de zinco dopado com alumínio, uma camada intermédia de óxido de molibdénio e por um eléctrodo de prata. O objectivo deste trabalho foi o estudo e a caracterização das propriedades electrónicas da interface MoO_x / ZnPc: C_{60}. Para este propósito recorreu-se à análise por espectroscopia fotoeléctronica ultravioleta (UPS) para a caracterização dos níveis electrónicos de valência enquanto que para sondar os níveis electrónicos perto do núcleo utilizou-se a espectroscopia fotoelectrónica por raios X (XPS). A banda de valência e os valores da função trabalho da interface MoO_x / ZnPc: C_{60} foram caracterizados em função da espessura da camada de MoO_x e em função da temperatura de recozimento. As curvas corrente-voltagem (IV) foram medidas em função da temperatura de recozimento e as propriedades ópticas da camada de MoO_x foram determinadas por transmissão na gama de 250-2500 nm. A espectroscopia de absorção de raios X perto da descontinuidade de absorção (NEXAFS) foi também utilizada para esclarecimentos adicionais sobre a situação da estrutura electrónica recorrendo-se à radiação de sincrotrão (sincrotrão BESSY II, Berlim, Alemanha).

Abstract

The search for low cost photovoltaics has led to the use of organic materials as possible candidates to substitute silicon based solar devices. Organic materials have high absorption coefficients, allowing the use of very thin films and low cost solution phase manufacturing techniques. Control over the electronic structure of organic/inorganic semiconductor interfaces is a key step for the development of these devices. In the present study this issue is addressed for an organic solar cell with an inverted structure: an organic absorber layer of zinc phthalocyanine: Fullerene heterojuntion, sandwiched between a front electrode of zinc oxide doped with aluminium, an intermediate buffer layer of molybdenum oxide and a silver electrode. The objective of this experimental work has been the investigation of the electronic properties of the MoO_x/ZnPc:C_{60} interface. For this purpose photoelectron spectroscopy using different types of radiation has been carried out. Results will be presented on the interface analysis carried out by ultraviolet photoelectron spectroscopy (UPS) for the study of the valence electron levels and by X-ray photoelectron spectroscopy (XPS) to probe the core electron levels. Valence band offsets and work function values at MoO_x/ZnPc:C_{60} interfaces have been characterized as a function of MoO_x thickness and as a function of annealing temperature. Current-voltage characteristics (I-V) were measured as a function of annealing temperature and the optical properties of the MoO_x layer were measured by transmission in the range 250-2500 nm. Near edge X-ray absorption fine structure (NEXAFS) spectroscopy was used to give additional insight into the situation of the electronic structure: spectra were taken from the electron storage ring for synchrotron radiation (BESSY II, Berlin).

1 Introduction

The limited supply of today's main energy sources in the form of oil, coal, natural gas and uranium and the increasing global concern over the issue of climate change have focused research attention on alternative, renewable energy sources, of which photovoltaics (PV) is a promising example.

Sun delivers in fact more power than the whole mankind needs. Considering the radiation emitted by the sun, the earth's radius r and the area A of the earth, the sun radiation on earth can be calculated:

Radiation: 1'368 W/m^2 (solar constant) , r = 6'370 km (6.370 x 10^6 m) and A = $r^2 \times \pi$= (6.370 m $\times 10^6$)^2 $\times$ 3.1415 . The radiation on earth is thus 1.74 $\times 10^{17}$ Watt [1].

Currently silicon solar cells dominate the PV market, as they have demonstrated high efficiency (up to 25%) [2], due to the excellent charge transport properties and environmental stability of high purity silicon. However, the methods used to manufacture high effienciency silicon solar cells are costly and have thus prevented PV from supplying a significant portion of the world's energy.

The search for low cost PV has led researcher to organic materials as possible alternative candidates.

After the discovery of polymer with both conductive and semiconductor properties in 1906 [3], such materials have been intensively studied for different PV applications.

Organic photovoltaics (OPV) has been developed rapidly in the past decade because they can be produced using solution phase techniques, such as ink jet printing or coating using roll-to-roll (R2R) machinery, thus allowing for fast, simple, low-cost and large-volume processing. The potential speed and simplicity of OPV processing is unmatched by other current technologies. Additionally, organic semiconductors have very high absorption coefficients [4], which allow very thin films to be used, whilst still absorbing a sufficient portion of the solar spectrum.

Extensive research over the last 5 years has produced marked increases in the efficiency of OPV devices. The current certified record of power conversion efficiency is 12 % [5].

A solar cell is considered organic if the active absorbing layer comprises only organic materials; for other layers, metals and other inorganic materials can be used. The OPV field also includes a category of hybrid solar cells, in which the active layer also contains an inorganic component such as quantum dots or nanostructured inorganic metal oxides mixed with coniugated polymers [4].

Control over the electronic structure of organic/inorganic semiconductor interfaces is required to produce hybrid solar cell devices with tailored opto-electronic properties.

The key issue for the commercialization of optoelectronic devices based on organic semiconductors is in fact the energy level alignment at contacts between the photoactive organic layer and the inorganic buffer layer or the electrodes.

In most devices, charges have to be transported across such interfaces, and therefore low charge injection barriers are required. The electrochemical mechanism governing the energy level alignment at organic/inorganic interfaces is important for further progress in the field. A way to align the energy levels to each other might be the search for molecule-semiconductor pairs with appropriate energy spectrum. However, such search is made intricate by the fact that the ionization potential and electron affinity of the isolated molecule can not be used as references, because their quantities are modified by the specific intermolecular and molecule-substrate interactions occuring in contact with another material.

In this work, this issue is addressed for the interface between the inorganic buffer layer of molybdenum oxide and the organic photoactive layer of zinc phthalocyanine doped with carbon fullerene C_{60}.

The interface characterization is carried out using photoelectron spectroscopy with Ultraviolet (UPS) and X-ray (XPS) radiation. Further experimental techniques, such as optical UV-VIS measurements and current-voltage analysis are used to better characterized the interface.

1.1 Device structure and operating principles

The main distinction in the working principle of the OPV as compared to inorganic PV is that when a photon is absorbed in the inorganic material, free charge carriers are created, for example, in a silicon solar cell, an incident photon excite an electron from the valence band, thus forming an electron-hole pair. Due to the crystalline nature of the silicon lattice, these charge carriers experience only a small force of interaction, that is, absorption in silicon leads to effectively free charge carriers. Due to the low relative dielectric constant of organic semiconductors (ε_r= ~3), there exists a large electrostatic force between electrons and holes [4]. When a photon is absorbed in the organic material, an excited electron-hole pair is formed, where the electron and hole are coulombically bound. This excited state is referred to as an "exciton" [6]. A force is needed to overcome this excitonic binding energy so that free charge carriers can be created and transported throughout the device. The force needed to overcome the exciton binding energy is given by the energy level offset of the lowest unoccupied molecular orbital (LUMO) of the donor and the acceptor material. This energy offset used to dissociate excitons is denoted as Δ_{ES} in Fig.1.1, which is the

excited state energy offset.

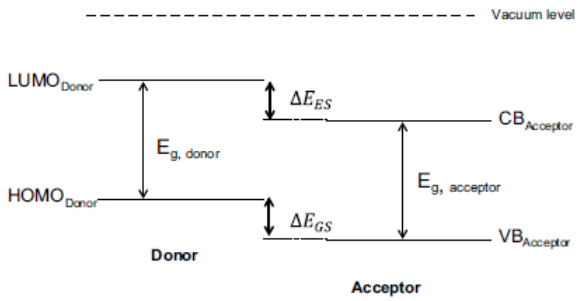

Figure 1.1 General energy band diagram of the heterojunction in a hybrid solar cell [4].

The photoelectric conversion mechanism in OPV can be summarized as follows: when a photon is absorbed in the donor material an electron is "promoted" to the lowest unoccupied molecular orbital (LUMO), while leaving the positive charge carrier, in the highest occupied molecular orbital (HOMO). The excited pair is still bound by coulomb attraction forces forming an exciton. The exciton diffuses to the interface of the donor and acceptor material, and is dissociated at the donor-acceptor interface into free carriers. Once separated, the electron can transfer to the acceptor material at an interface and be transported to the cathode for charge collection. The hole produced in the donor material travels throughout the polymer and is collected at the anode [4]. This mechanism is displayed in Fig.1.2.

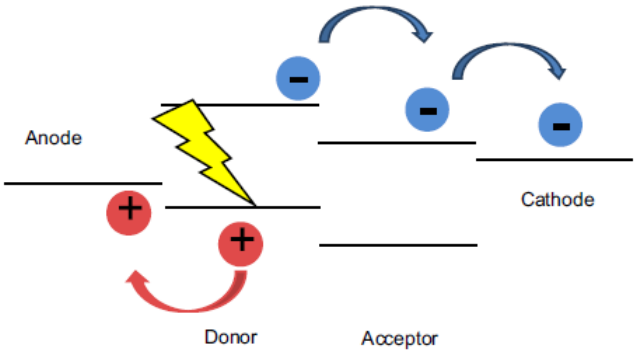

Figure 1.2 Schematic diagram presenting the charge transfer for a photo generation in the electron donor material [4].

The free charge collection at opposite electrodes is achieved by the asymmetric ionization energy or work function of the electrodes.

It is well established that the charge transport in organic materials occurs via a process of hopping between energy states and is affected by traps and recombination sites in the photoactive film [4].

The common structure of the organic solar cells comprises a multilayer stack. Usually the active layer, which is a combination of donor and acceptor materials, is sandwiched between two electrodes. A discrepancy between the work function of the anode and cathode electrode material is required to provide a direction for the photocurrent. One of the electrodes needs to be transparent for illumination of the cell. Buffer layers are applied between the electrodes and the active layer to ensure charge-selective transport [7].

Due to the small excitonic diffusion length n, conjugated polymers (~10 nm), bi-layers structures are limited in excitonic dissociation, as there exist only one interface, that is, only the photons absorbed by a very thin layer next to the interface can contribute to the photocurrent while the rest is lost throught recombination mechanisms [8]. In order to increase the heterointerfacial area and thus excitonic dissociation, the donor and acceptor material can be mixed in a bulk, forming a nanoscale morphology, called a bulk heterojunction device structure. In this way, the interface is extended throughout the whole active layer, and the device requires smaller exciton diffusion lengths, providing more efficient charge separation and separate paths for the transport of the free carriers.

1.2 Photovoltaic performance characteristics

In this chapter, complete solar cells with the structure ZnO:Al/ZnPc:C_{60}/5 nm MoOx/Ag have been characterized by means of current-voltage J(V) and temperature dependent current-voltage J(V,T) measurements.

Current-voltage (I–V) measurements are the most common tool for solar cell evaluation and characterization.

To allow for valid comparision of device performance, an international standard for input power is used. This standard is an incident spectrum of AM 1.5 G, which can be approached by commercial solar simulators, with an intensity of 1000 W/m^2, whilst the cell is at a temperature of 25°C.

1.2.1 Electrical model

Fig. 1.3 shows an equivalent circuit model which is commonly used to interpret the characteristic of PV devices. The solar cell in the dark acts as a simple diode: the current-voltage relationship

follows the exponential relation of the pn-junction:

$$J(V) = J_0(e^{qV/AkT} - 1)$$

Eq. 1.1

where k is the Boltzmann constant, T the temperature, V is an external applied bias voltage, J(V) the current density, A the diode quality factor and q the elementary electric charge (J(V) is obtained by dividing the current to the device area) [9].

For a better description of a real device, resistive losses have to be added into this equation: A series resistance R_S and a shunt resistance R_{SH}. Additionally, a photo-generated current density J_L has to be introduced into the equation to describe the device under illumination (in the dark J_L =0). In thin film solar cells, J_L may depend on the applied bias voltage. The so-called 1-diode model describing the current-voltage characteristic of a solar cell is given by the following equation:

$$J(V) = J_0 \left[exp(\frac{q(V - R_S J(V))}{AkT}) - 1 \right] + \frac{V - R_s J(V)}{R_p} - J_L$$

Eq. 1.2

where J(V) accounts for the current density flowing through the device which is the sum of the current density flowing through the diode (first term), the current density flowing through the parallel resistance (second term) and the photo-generated current density (last term) [10].

The illuminated cell behavior can be related to that of a diode parallel connected with a current source R_S, these connected in series with a shunt resistance R_{SH}.

- The diode D takes into account the current losses due to recombination in the interior of the cell. D has an ideality factor n and a saturation current I_0 (current in the dark at reverse bias);
- The current source is equivalent to the photo generated current due to the PV effect I_L;
- R_S takes into account all the resistances at interface in the layers, the conductivity of the semiconductors, and the electrodes;
- R_{SH} takes into account the leakage of the current through shunts as a result of defects in the films. (For good performance of the OPV device, R_s needs to be low and R_{sh} to be high);

- Solar cell voltage V: The cell can generate a voltage between 0 and Voc depending on the size of the load resistor. In order to obtain IV curve data in other voltage ranges (V $<$ 0 and Voc $<$ V) in the IV curve an external voltage source is required [10].

The current-voltage characteristic for a typical solar cell, when light is shone on the device, becomes a superposition of the dark J-V with the light-generated current with the curve shifted by a quantity equal to the current that is generated by the cell (Fig.1.3).

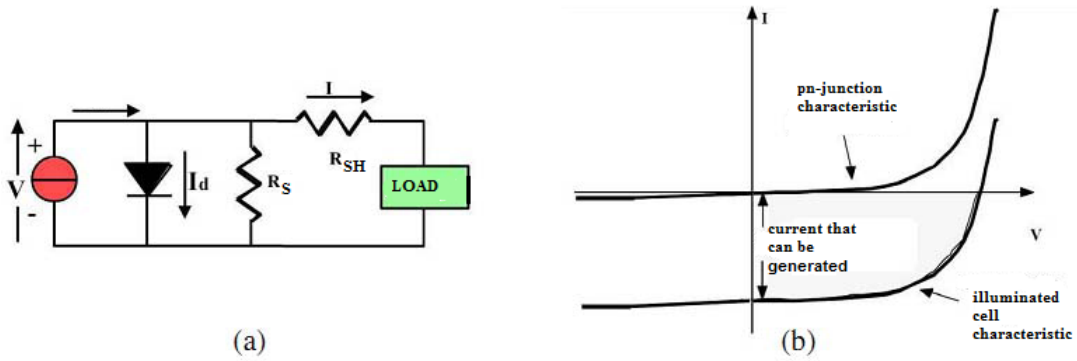

Figure 1.3 a) Equivalent electrical circuit and b) characteristic of the dark and illuminated solar cell [9].

The characteristic curve of a illuminated solar cell can be presented by considering only the fourth quarter of the graph and with inverted current verse. This facilitates the determination of the basic parameters.

In Fig. 1.4 the fourth quarter of the characteristic curve is displayed, the green curve represents the power generated by the solar cell.

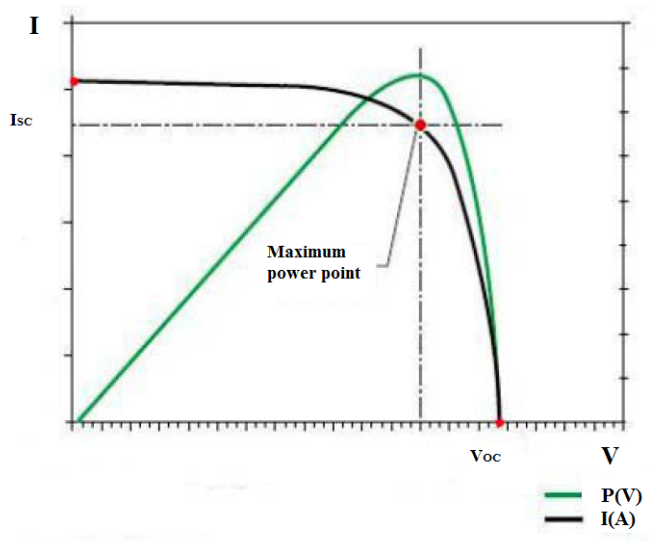

Figure 1.4 Current-voltage characteristic for a generic illuminated solar cell. [9].

J–V characterization means determination of the basic parameters: the open circuit voltage V_{OC}, the short-circuit current J_{SC}, the fill factor FF, and efficiency (η) which are determined by only three points on the J–V curve and are briefly described below.

1.2.2 Power conversion efficiency

The power conversion efficiency (PCE) of a solar cell is defined as:

$$PCE = \frac{J_{SC} \times V_{OC} \times FF}{P_{in}}$$

Eq. 1.3

where J_{SC} is the short circuit current density, V_{OC} is the open circuit voltage, FF is the fill factor and P_{in} is the power of the incident light [10].

1.2.3 Fill factor

The fill factor describes the "squareness" of the J-V curve. It is the ratio between the maximum product of J and V and the product V_{OC} and I_{SC}.

$$Fill\,factor = \frac{J_m \times V_m}{J_{SC} \times V_{OC}}$$

Eq. 1.4

thus

$$P_{max} = (JV) = V_{OC} \times J_{SC} \times FF$$

Eq. 1.5

where J_m and V_m are the maximum power point current density and voltage, respectively [10].

The higher the FF the more the J-V characteristics resembles a constant current source with a maximum voltage and the higher is the electric power that can be extracted. The voltage-current (V_p, I_p) combination that gives the largest power rectangle is called the maximum power point.

Due to physical constraint on diode quality, the practical limit to the fill factor is less than the ideal value of 1 [4].

1.2.4 Open circuit voltage

V_{OC} can than be derived quantitatively using:

$$V_{OC} = \frac{nkT}{q} ln(\frac{I_L}{I_0} + 1)$$

Eq. 1.6

In contrast to silicon p-n junction solar cells, the origin of the open circuit voltage in bulk heterojunction devices is still not completely understood. Multiple reports have investigated this property for OPV devices. In 2001, Brabec et al. [11] proposed an effective band gap model for bulk heterojunction cells, whereby the maximal value of V_{OC} is related directly to the energy difference between the HOMO level of the donor and the LUMO level of the acceptor.

In 2006 a report studied the relationship between the energy levels of the donor-acceptor blend and the V_{OC} for bulk heterojunction devices [12]. It was found that there exists a linear relationship

between the HOMO position, which is related to the band gap of the heterojunction, and the V_{OC}. This relationship between the HOMO of the donor material and the V_{OC} of the device was found:

$$V_{OC} = (\frac{1}{e}(\left|E^{Donor}HOMO\right| - \left|E^{Acceptor}LUMO\right|) - 0.3V$$

Eq. 1.7 [4]

1.2.5 Short circuit current density

The short circuit current density J_{SC} is the maximum photocurrent density which can be extracted from the device at short circuit conditions.

The J_{SC} is directly related to the external quantum efficiency (EQE), which is defined as the ratio between the number of electrons on the external circuit and the number of incident photons at a specific wavelenght.

J_{SC} can be expressed as [4]:

$$J_{SC} = \frac{q}{hc}\sum\int_{\lambda min}^{\lambda max} EQE \times P_{in}(\lambda)\lambda \times d\lambda$$

Eq. 1.8

For the operation of a hybrid solar cell, EQE is dependent on five major steps, each of which has some associated efficiency. Thus, it can be expressed as [4]:

$$EQE = \eta_{abs} \times \eta_{diff} \times \eta_{diss} \times \eta_{tr} \times \eta_{cc}$$

Eq. 1.9

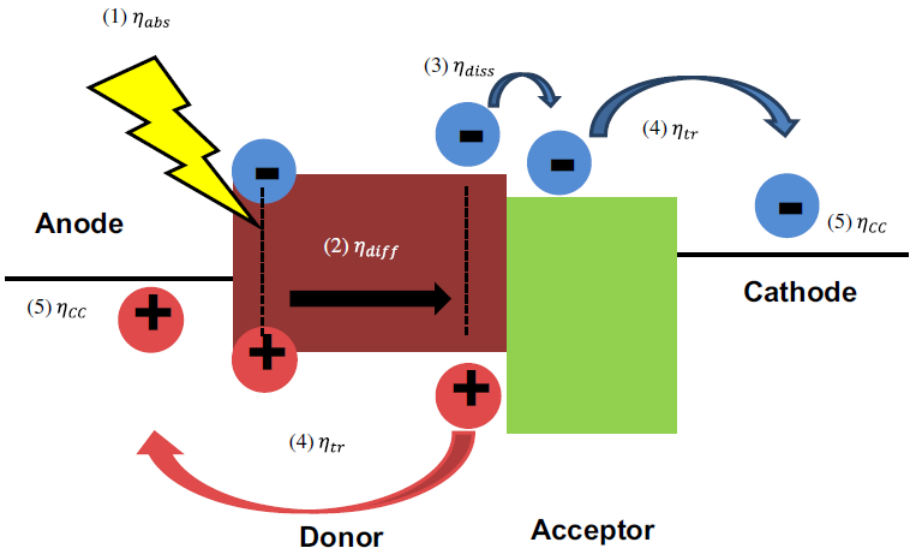

Figure 1.5 Energy band diagram illustrating the five steps in the charge transfer process. The efficiency of these steps determines the EQE of the hybrid device [4].

The parameter η_{abs} describes the absorption yield of the device, which is displayed as (1) in the Fig. 1.5. The absorption spectrum of the material is determined by both the band gap and absorption coefficient of the material, whilst the thickness of the photoactive layer will also affect the absorption yield [13].

The parameter η_{diff}, displayed in Fig. 1.5 as (2), describes the ability of an exciton to diffuse to a donor-acceptor interface. This parameter depends on both the excitonic diffusion length, which is a material property, and the distance between excitation and the nearest interface, which is related to the nanoscale design of the photoactive layer. As the excitonic diffusion lenght in conjugated polymers is very low [14], control over the D-A morphology is important for successful exciton diffusion.

The parameter η_{diss}, displayed in the Fig. 1.5 as (3), is the exciton dissociation yield. The energy offset, required to allow conduction to occur, must be larger than the excitonic binding energy in the material to facilitate charge transfer. This energy is typically in the range of 0.1-0.5 eV [14].

The parameter $\eta_{tr}(4)$ describes the efficiency of charge carrier transport throughout the device.

The parameter η_{cc}describes the efficiency of charge collection at the electrodes. This represents the ability of the charge carriers to be injected into the electrodes from the photoactive layer. The success of this step is dependent on the electronic composition of the device.

2 Materials

The choice of materials in OPV is crucial to the overall efficiency and thus the success of this technology. This section describes the materials which have been used in this research work and their respective functions in the solar device. The solar cell structure used in this work is of an inverted type, where the cathode is the transparent front electrode and the anode the back electrode.

The complete structure of the solar cell investigated in this work is:

Zinc oxide doped with aluminum as front electrode, zincphthalocyanine mixed with Buckminster carbon fullerene as photoactive layer, molybdenum oxide as intermediate buffer layer and silver contacts as back electrodes.The device is built on a glass substrate.

The mixed layer of ZnPc and C_{60} deposited in this experimental work presents an aggregation of small grains of both donor and acceptor contacting materials with dimensions below the excitons diffusion lenght.

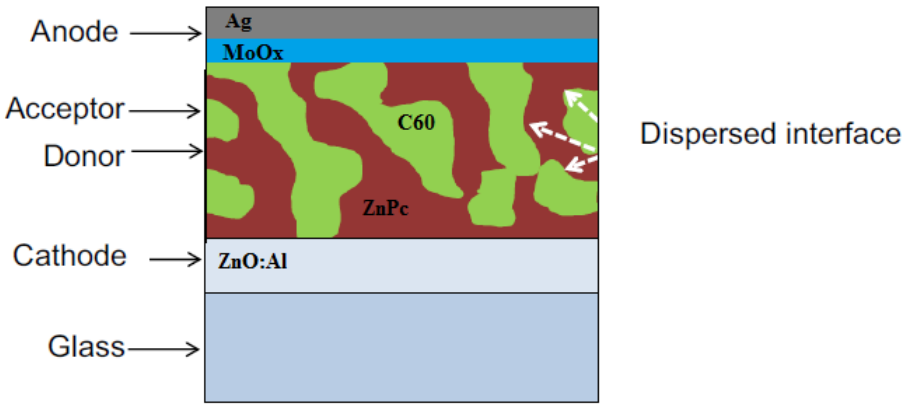

Figure 2.1 Schematic bulk heterojunction structure for the inverted solar cell used in this work.

2.1 Substrate and front electrode

Glass is by far the most reported substrate because of its low cost and stability in almost any subsequent treatment and was therefore chosen as substrate.

With respect to the transparent electrode, ITO has been the almost exclusive choice, given its excellent properties as hole conductor, but due to the scarcity and the cost of indium, which

by weight is the main material in ITO, the need for new transparent semiconducting materials is growing.

In this work, a zinc oxide layer doped with aluminium is used as a low work function window cathode. The function of the cathode is to collect electrons from the device and here contributes as well to the device stability, as oxygen and water molecules are blocked by the ZnO:Al layer [4]. When doped with aluminium ZnO is a n-type contact. ZnO can be formed using a variety of synthesis methods and exhibits high electron mobility; furthermore it has a proven suitability of forming structurally well-defined hybrid structures with various conjugated organic molecules [15].

2.2 The intermediate layer

Absorber/electrode interfaces in OSC are optimized either by the electrode surface treatments or, as in this work, by insertion of an intermediate or buffer layer [16].

The intermediate layer has the function to selectively transport one type of charge (negative or positive) while simultaneously blocking the opposite charge, decreasing in this way the probability of charge recombination.

Furthermore, intermediate layers are used to bridge a mismatch of energy levels between the active layer and an electrode, improving in this way the alignment of the energy levels. The intermediate layer even compensates for the roughness that electrodes have and that might result in shunts in the film, removing some of the shunts. The intermediate layer used in this work follows an anode and is thus used as hole conductor and electron blocking layer. As hole conductor the most widely used electron-blocking material has been polyethylenedioxythiophene:polystyrenesulfonate (PEDOT:PSS) but the substitution of PEDOT:PSS with stabler materials can significantly improve the device´s stability. In this work a hole conductor buffer layer of MoO_3 has been used. This oxide has been progressively investigated in the last years due to its supposed appropriate work function values and band alignment when inserted between the photoactive layer and the electrode. It has been in fact experimentally found that molybdenum oxide as the interfacial modification layer in OSC improves the transport mechanism of the solar cell [17].

Recently, transition metal oxides, such as molybdenum oxide MoO_3, vanadium oxide V_2O_5, and tungsten oxide WO_3 have attracted much attention for organic solar cells application due to their suitable electronic properties and charge generation ability for organic solar cells. Recent works [36,37] reported how the presence of MoO_3 layer at the organic/metal interface significantly reduces the contact barrier and provides protection from diffusion and other chemical reactions between the

organic layer and the metal.

MoO_3 presents highly efficient charge injecting (or extracting) properties, improved stability, high transparence and compatible easy- fabrication process (thermal evaporation) and therefore has been here chosen as intermediate buffer layer.

Furthermore the oxide films of MoO_3 can be deposited by thermal evaporation, which is compatible to thermal evaporation of Au anode, used in this experimental work [38].

In this work the work function energy levels of the MoO_3 at the interface with the organic layer is investigated. In fact, despite numerous papers related to the application of transition metal oxides as buffer layer in organic electronic devices, the underlying physical mechanisms pertaining to their electronic structure remain not completely defined.

2.3 The active layer

The active layer used in this work consists of a bulk heterojunction of buckminster fullerene C_{60} as acceptor material and zinc phthanolocyanine (ZnPc) as the donor material.

2.3.1 Fullerene

The fullerene's role as an electron acceptor and in providing a continuous network for electron transport in polymer and small molecules blend devices is well established [18].

This molecule is very stable and can be easily evaporated in vacuum conditions. The absorption coefficient α of C_{60} is $0.8 \cdot 10^5$ cm^{-1}. C_{60} is considered an optimal acceptor material for organic solar cell due to its high acceptor properties [8]: the transport of an electron from a donor molecule next to a C_{60} molecule takes place in about 40 fs [8].

2.3.2 Donor material

Phthalocyanine ($ZnC_{32}H_{12}N_8$) Fig.) has been used as photoactive donor material. ZnPc molecules are easy and cheap to synthesize. ZnPc has an absorption coefficient α of up to $1.5 \cdot 10^5 cm^{-1}$, being thus an optimal absorber material in the visible region, from 550 to 750 nm [8]. The molecules are small and stable enough to be thermally evaporated. The hole mobility μ of ZnPc is about 0.02 cm/Vs, the molecules are considered as p-conductor.

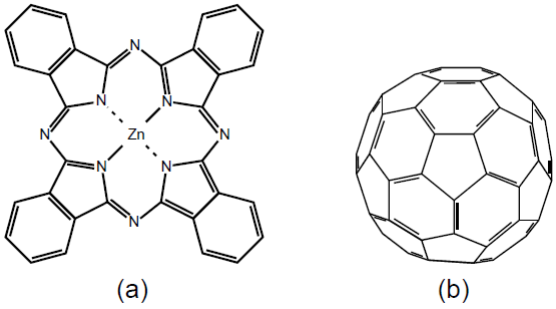

Figure 2.2 Chemical structure of (a) zinc phthalocyanine and (b) fullerene C_{60} [8].

2.4 The back electrode

The back electrode is the final layer that completes the device structure. Similar to the front electrode, the use of high or low work function metals defines the operation of the back electrodes as anode or cathode, respectively. The electronic properties of the latter electrode must match with those of the organic absorber layer. Particularly, for an effective collection of the charge carriers from a single organic layer, the work function of the metallic is adjusted to the HOMO/LUMO level of the donor/acceptor material for the formation of an ohmic contact. In the case of absorbers from blend structures effective charge-selective electrodes are required. These are achieved by the fine adjustment of the electrode work function by allowing low and high work function conducting materials. Depending on the desired work function of the back electrode, different metals are use. Aluminium, silver and gold are the most commonly used. Here physically deposited silver contacts are used.

2.5 Final structure

A schematic overview of the complete solar cell, with inverted structure, used and investigated in this work is presented in Fig. 2.3.

In an inverted cell, the electric charges exit the device in the opposite direction as in a normal device. The positive and negative electrodes, which absorb the negative and positive charges, respectively, are reversed. Inverting the device architecture allows to make the cathode out of a more suitable material, which can provide effective protection to the polymer layer. [19].

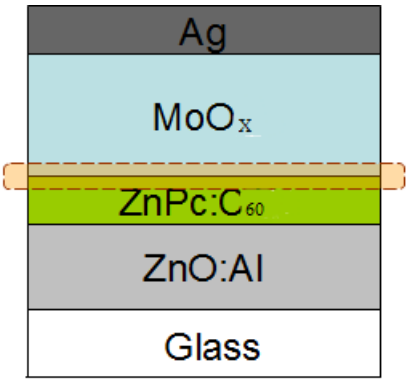

Figure 2.3 Schematic overview structure of the solar cell with ZnPc and C_{60} as photoactive layer. The investigated interface is shown.

3 Surface characterization techniques

Photoelectron spectroscopy (PES) is a surface sensitive investigation method and one of the most useful technniques of modern surface material science. This technique is based on the photoelectric effect discovered by Heinrich Hertz in 1887 [20]. A photon transfers its energy to the atom thus exciting electrons to upper energy levels, from which they can be ejected from the material. From the energy distribution of the photoelectrons, which is probed in an electron energy spectrometer, the fundamental energy levels and excitation energies of the atoms in a sample are determined. Different energy ranges provide different information: electrons emitted from core levels furnish information about the presence and, to a certain degree, the concentration of elements in the sample. Furthermore, the chemical environment can also be determined, i.e. the oxidation state of the element in question and as well as its first coordination shell may also be determined from the spectra. Electrons from valence levels give information about the electronical band structure of the material.

Photoelectron spectroscopy requires vacuum operating conditions. The electrons emitted from the sample should meet as few gas molecules as possible on their way to the analyser so that they are not scattered and thereby lost from the analysis. Furthermore these techniques are higly surface-specific, with sampling depths tipically of a few atom layers. Most of the electrons originate from the first atom layers. Even very small amounts of contamination can affect the experiment. Since the principal source of contamination comes from the residual gas in the operating chamber, the system must operate under ultra-high vacuum (UHV) conditions. In fact a monolayer of gas will accumulate on a surface in about 1.5 s at a pressure of 10^{-6} torr and at room temperature, if every molecule hitting the surface stays there on impact. If, as typical requirements, no more than 0.05 atom layers of contaminant should accumulate in the space of 30 min, then, gas kinetics rule that the residual gas pressure should be $4 \cdot 10^{-11}$ torr.

Furthermore UH vacuum is needed to extend the life of X-ray and electron optics in the vacuum system.

3.1 UPS

Low energy photons may be used to excite electrons in the solid. In ultra-violet photoelectron spectroscopy (UPS) the source of photons is a differentially pumped inert gas discharge lamp. This produces discrete low energy resonance lines: He I 21.2 eV, and He II 40.8 eV. Since there is only

sufficient energy to emit electrons from the valence band, the technique is used in the study of the electron band structure of solids and not for analytical studies.

3.2 XPS

X-ray photoelectron spectroscopy is a surface chemical analysis technique, also referred to electron spectroscopy for chemical analysis (ESCA), used to analyze the surface chemistry of a material in its "as received" state and can be addressed to a wide variety of samples. XPS was developed in the mid-1960's by Kai Siegbahn and his research group at the University of Uppsala, Sweden.

XPS detects all elements with an atomic number Z of 3 and above.

Surface analysis by XPS is performed by irradiating a sample, in a vacuum environment, with monochromatic soft X-rays. They interact with the inner-shell electrons of an atom in the surface region of the material of about 1-10 nanometers by the photoelectric effect and cause electrons to be ejected. The kinetic energy of the emitted photoelectrons provides information about the binding energy of the electron in the material. The basic equation of XPS is

$$E_k = hv - BE - \phi_s$$

Eq. 3.1

where hv is the energy of the incident photon (h is the Planck's constant and v the X-ray frequency), BE is the binding energy of the atomic orbital from which the electron originates, and ϕ_s is the spectrometer work function, which is found by calibration [20].

The kinetic energy E_k of the photoelectron is measurable then the binding energy BE can be calculated. XPS spectra represents the intensities of the photoelectrons versus BE or E_k. Since each element has a unique binding energy, the energy of the photoelectrons is related to the atomic and molecular environment from which they originated. The number of electrons emitted is related to the concentration of the emitting atom in the sample.

X-rays are created by accelerating high energy electron beam (~15keV) onto an anode material (typically Mg and Al). The electron beam creates holes in the core level of the anode material and electrons from outer shells fill up the holes emitting characteristic X-ray radiation. If Mg is used as anode material the created X-rays (Mgk_α) have an energy of 1253.6 eV, while with Al, the radiation (Alk_α) has an energy of 1486.6 eV.

The relaxation of the excited state due to photoemission, can occur via emission of radiation (fluorescence radiation) or by emission of an additional electron (Auger electrons). In this process, as shown in Fig. 3.1 , an outer electron falls into the inner orbital vacancy, and a second electron is emitted, so that the Auger electron has kinetic energy equal to the difference between the energy of the initial ion and the doubly-charged final ion. Since the Auger process contains three steps, the kinetic energy of the Auger electron depends only on those thress electronic levels and not on incident X-ray photon energy.

The electron signal in XPS includes contribuitions from both photoelectron and Auger electron lines.

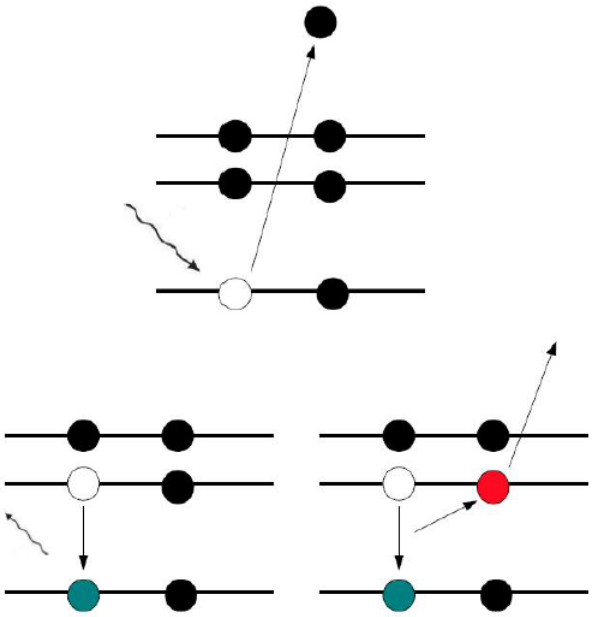

Figure 3.1 Diagram of the photoelectric process (top) and the Auger process (bottom) [21].

The information depth in XPS is related to the distance an electron can pass through the matter.

This average distance that an electron can travel between successive impacts without modifying its direction or energy or other particle properties is called the inelastic mean free path of an electron.

The probability of interaction of the electrons with matter far exceeds those of the photons, so while the path lenght of the photons is of the order of micrometers, that of the electrons is of the order of tens of angstroms. Thus, even if ionization occurs to a depth of a few micrometers, only those electrons that originate within tens of angstrom below the solid surface can leave the surface without energy loss. It is these electrons that produce the peaks in the spectra and are useful for

the analysis. The inelastic mean free part λ of the electrons in the regime between a few eV and many hundred eV is plotted in Figure 3.2. The dashed curve shows a calculation of the inelastic mean free path independent of the material and the points are measured data from many elemental solids. The data points scatter more or less around the calculation. The curve is therefore often called a universal curve. The reason for this universality is that the inelastic scattering of electrons in this energy range is mostly involving excitations of conduction electrons, which have more or less the same density in all elements. The mean free path curve has a minimum around a kinetic energy of about 70 eV. There the mean free path is less than 10 Å. This means that a detected electron with this kinetic energy which has left the solid without suffering an inelastic scattering event must originate from the first few layers.

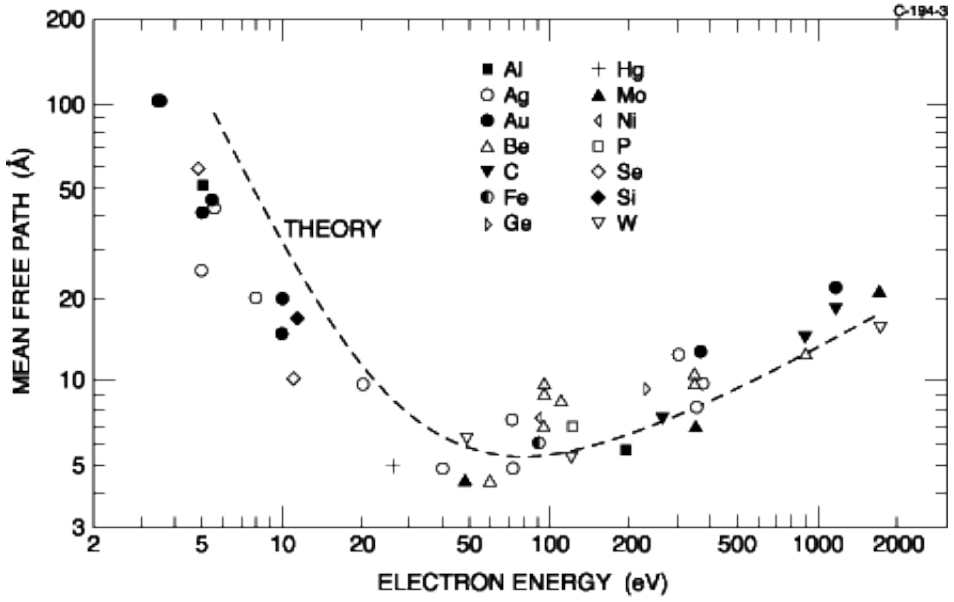

Figure 3.2 The mean free paths of the electrons in solid [21].

3.3 Synchrotron

A further source of photons used for spectroscopy analysis is the synchrotron radiation. Synchrotron radiation is an electromagnetic radiation emitted from deflected charged particles moving at relativistic velocities.

Classically, any charged particle which moves in a curved path or is accelerated in a straight-line path emits electromagnetic radiation. Various names are given to this radiation in different

contexts, in the application to circular particle accelerators like synchrotrons, where charged particles are accelerated to very high speeds, the radiation is referred to as synchrotron radiation. Electrons circulated continuosly in a storage ring (BESSY II, Berlin) produce a continuous spectrum of photons with energies from few electronvolts to several kiloelectronvolts [20]. With a monochromator a variable energy photon source is provided. As a consequence of relativistic motion, the radiation is emitted in a narrow cone in the forward direction from a point like source. At BESSY II, Berlin, the electron's energy is 1.7 GeV and synchrotron radiation is generated from magnetic deflections in simple electromagnetic bending magnets, from undulators consisting of long magnetic rows of permanent magnets as well as from superconducting magnet structures like wavelength shifters and multipole wigglers.

Synchrotrons consist of large circular magnets positioned around the circumference of the circle. Magnets ensure that the electrons may circle in the storage ring. The main components are the dipoles, the quadrupoles and the sextupoles. The dipoles enable the circular orbit of the electrons. The quadrupoles compensate the natural behavior of electrons to drift apart. Sextupoles make small corrections on the quadrupoles and are important for storing the beam over a longer period of time.

Acceleration of the charged particles is achieved by the application of radio frequency electric fields at rf (radio-frequent) cavities along the circumference of the ring. The magnetic fields must be increased synchronously with the acceleration in order to keep the particles on the constant radius path.

The accelerators can be used with protons, electrons and even with heavier positive ions.

For surface chemical analysis electrons are used because they are relatively easy to accelerate due to their high electric charge and their small mass.

The energy radiated from the electrons is proportional to the fourth power of the particle speed and is inversely proportional to the square of the radius of the path. It becomes the limiting factor on the final energy of particles accelerated in electron synchrotrons.

The classical formula for the radiated power from an accelerated electron is

$$P = \frac{2Ke^2a^2}{3c^3}$$

Eq. 3.2

which is the Larmor formula, used to calculate the total power radiated by a non-relativistic point charge as it accelerates, where a is the acceleration, e is the charge, and c is the speed of light.

For a non-relativistic circular orbit, the acceleration is just the centripetal acceleration, $\frac{v^2}{r}$.

The orbits of interest in accelerators are higly relativistic, so the relativistic acceleration can be calculated from

$$a = \frac{1}{m}\frac{dp}{d\tau} = \frac{1}{m}\gamma\frac{d(\gamma m\nu)}{dt} = \gamma^2\frac{d\nu}{dt} = \gamma^2\frac{\nu^2}{r}$$

Eq. 3.3

where $\tau = \frac{t}{\gamma}$= proper time,

$$\gamma = \frac{1}{\sqrt{1-\frac{v^2}{c^2}}}$$

is the Lorentz factor and m is the rest mass of the particle [39, 40].

The radiated power is then

$$P = \frac{2Ke^2}{3c^3}\left[\gamma^2\frac{\nu^2}{r}\right]^2 = \frac{2Ke^2\gamma^4\nu^4}{3c^3r^2}$$

Eq. 3.4

Since the velocity in synchtrons becomes nearly constant for highly relativistic particles, the term γ^4 becomes the dominant variable in determining loss rate. This means that the loss scales as the fourth power of the particle energy.

For an accelerator like a synchrotron, the radius is fixed after construction, but the inverse dependence of synchrotron radiation loss on radius argues for building the accelerator as large as possible [39].

In BESSY II, where the Synchrotron's experiments have been carried out, before injection in the main storage-ring the beam is accelerated over a microtron and a synchrotron to its final energy of 1.7 GeV. The accelerating process takes 50 ms and can be repeated with a repetition rate of 10 Hz. The total current in the storage ring of 100 mA can be obtained by successive injection of electrons, accelerated in multiple accelerating cycles.

The amount of synchrotron radiation is proportional to the stored beam current. To keep the current high it is necessary to reduce the loss of electrons. BESSY II is designed to permit a life-time of 8 to 10 hours [41].

The synchrotron source is ideal for carrying out extended absorptrion spectroscopy (XAS), namely near edge X-ray absorption fine structure (NEXAFS) and extended X-ray absorption fine structure (EXAFS), by monitoring the fluorescence electron yield over the same photon energy range

in the region of the absorption edge.

The principle of NEXAFS measurements is the absorption of an x-ray photon by a core level of an atom in a solid and the consequent emission of a photoelectron. The resulting core hole is filled either via an Auger process or by capture of an electron from another shell followed by emission of a fluorescent photon. The difference between NEXAFS and traditional photoemission experiments is that in photoemission, the initial photoelectron itself is measured, while in NEXAFS the fluorescent photon or Auger electron or an inelastically scattered photoelectron may also be measured.

4 Experimental

4.1 Preparation of the samples

The samples used in this work were fabricated through the vapour phase deposition technique (VPD). In this chapter the principles of the VPD will be briefly described.

The samples were prepared on glass substrates coated with a transparent, conducting aluminum zinc oxide layer with a sheet resistance of 5 $\Omega/\square$. The thickness of the ZnO:Al film was about 920 nm and was measured with a Dektak-Kontakt-Profilometer. The organic layers of ZnPc:C_{60}, were deposited by the OVPD (Organic Vapour Phase Deposition) technique and the molybdenum oxide layer with the same VPD principle.

The following series of samples were prepared to study the interface between ZnPc:C_{60} and MoO_x.

- 2 x Glass/ZnO:Al
- 2 x Glass/ZnO:Al/ZnPc:C_{60}
- 10 x Glass/ZnO:Al/ZnPc:C_{60}/MoO_x
- 2 x Glass/ZnO:Al/MoO_x

The sample without the organic layer and/or the molybdenum oxide were studied as reference samples.

The average thickness of the MoO_x was approximately calculated about 100 nm. The SEM characterization of the profile of MoO_x on ZnO:Al images show an uniform and compact film of MoO_x(Fig. 4.1).

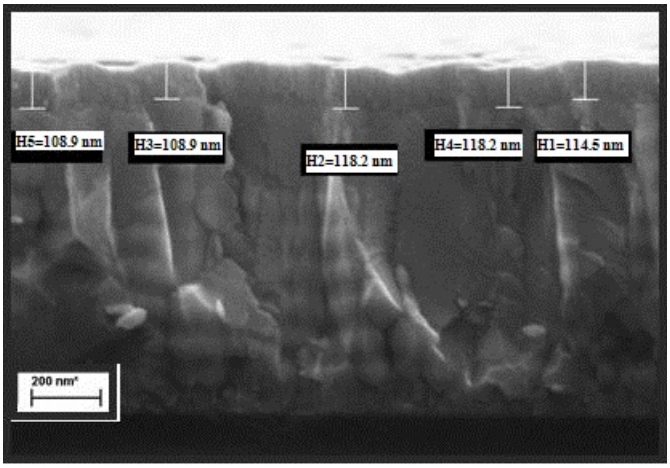

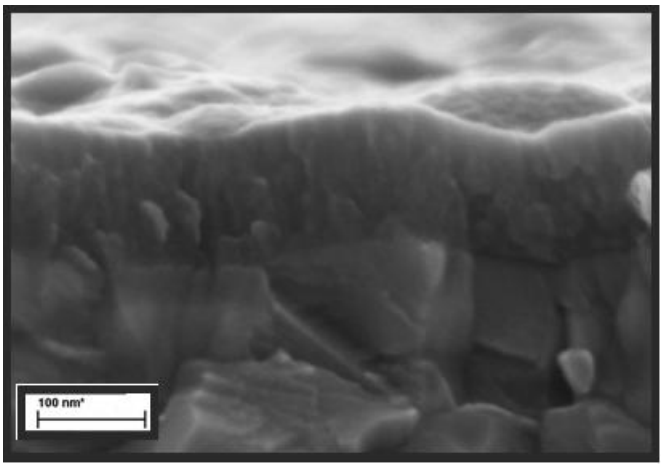

Figure 4.1 Scanning electron micrographs of the cross-section of physically deposited MoO_X on ZnO:Al. Shown in the first micrograph are the data used for evaluation of the thickness.

4.1.1 Organic layer deposition

The OVPD technique has been proved an useful method for the deposition of organic semiconductors devices [22]. Currently the most common used technique for the deposition of thin (<100 nm), molecular organic electronic devices is the vacuum thermal evaporation (VTE), which permits an high degree of purity. However, control of thin film uniformity and the mixing of multiple compounds into a single film, which is essential to the achievement of high performance devices, can be difficult using VTE, particularly for large-area substrates. In addition, in VTE a considerable fraction of the evaporant coats the cold walls of the deposition chamber; over time, inefficient materials usage results in a thick coating which can flake off, leading to contamination of the system and substrate.

Thin films produced by OPVD do not have problems related to contamination from the particles coming out of the walls of the chamber as they are warm and do not allow particles to stick. Due to the presence of the carrier gas, that becomes saturated with the vapours of the organic materials coming out from the source, the deposition occurs through an equilibrium process. VPD has been recently demonstrated as an alternative technique that eliminates the limitations of the VTE thus resulting in a rapid, particle-free, uniform deposition of organics on even large area substrates [23].

A schematic drawing of the OVPD method used in this work is shown in Fig. 4.2 [22]. The system is based on the commercial OVPD principle described in [23]. However, whereas in the OPVD system described in [23], the sources and the substrate are placed together into a hot wall horizontal quartz tube, in the OPVD system used here, the sources and the deposition chamber are

separated. Moreover, the deposition chamber of the OPVD system is provided with a close coupled showerhead with multiple orifices that acts as a gas distributor (Fig. 4.2). This allows an uniform injection of the organic molecules over the entire deposition area. The organic materials used in this work - ZnPc and the fullerene C_{60} - are thermally evaporated in special source containers in the presence of a preheated inert gas, N_2. The organic compounds are transported by the carrier gas through the deposition chamber. The stream then uniformly passes through the showerhead and condenses on the deposition area, consisting of a cooled substrate. Prior to their introduction in the showerhead orificies, the organic compounds in the gaseous phase are homogenised in a mixing chamber, being supplied from source containers mounted in separated furnaces. Each of the three furnaces mounted in the actual desing of the OPVD system used in this work, can hold multiple containers with different source materials. The deposition rate can be changed by changing the gas flow rate through external mass-flow controllers. Thus, the deposition runs can be performed at different source flows keeping at the same time a constant N_2 gas quantity, by adjusting the dilution pipe. The pipes are heated and always kept under continuous N_2 flow. In standby conditions, the sources are filled with N_2 and kept closed using valve B, while during the deposition process, valves B are off and valve A is open (Fig.4.2). Independently of the N_2 total flow, the deposition chamber pressure can be varied between 10^{-1} and 10^3 mbar.

The organic materials used wew C_{60}(MER Corp. Purity: 99,9%) and ZnPc (Alfa Aesar. Purity: 98%).

ZnPc:C_{60} layers were deposited at a deposition chamber pressure of 0,6 mbar. The source evaporation temperature was <500°C and the showerhead temperature was set at 425°C. The organic layer thickness was about 80 nm, the ratio 1:1 by thickness. The deposition rate was 0,483 Ang/s .The N_2 carrier gas quantity through each source (Q_{source}) was 500 ml/min and 283 ml/min for C_{60} and ZnPc respectively. Q_{total} was 1150 ml/min. The substrate temperature was 132 °C, the source temperature 436,7°C for C_{60} and 423,5°C for ZnPc. After the deposition process, the samples were transferred from the OPVD system through a N_2 filled glove box.

4.1.2 Buffer layer deposition

The buffer layers of MoO_x (Sigma-Aldrich, purity: 99,9%) were deposited with the same VPD principle as described above.

2,2 g of MoO_x powder were first put in the proper source container. In the deposition chamber was set a pressure of 4,4 $\cdot 10^{-7}$mbar. The rate deposition, measured by a quartz microbalance, was

0.5 Å/s and the substrate temperature was kept at room temperature.

4.1.3 Silver contacts deposition

The Ag contacts were deposited in the high vacuum chamber (base pressure~10^{-7}mbar) which is directly attached to the OPVD chamber, without exposing the corresponding absorber/metal interfaces to air. The high vacuum chamber is designed for deposition of solar cells metallic contacts as well as for charging/discharging substrates or complete solar cell devices into/from the OPVD system.

Further details about the OPVD setup can be found elsewhere [24].

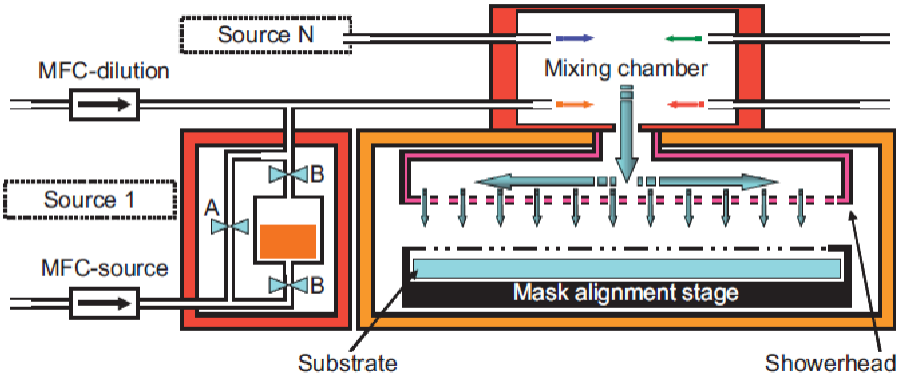

Figure 4.2 Schematic drawing of the OPVD apparatus [28].

4.2 Optical measurements

Transmittance and reflectance measurements were performed to monitor the band gap of the MoO_x layer. The optical spectra were taken for the bulk layer (100 nm). For thinner layers the performed measurements were not taken into account because the interference effects were too high to allow a significant data interpretation. For carrying out these measurements, samples were redeposited on quartz substrates due to the wider bandgap of glass.

Transmission and reflection measurements were carried out between 250 and 2500 nm at 25°C using a Perkin-Elmer Lambda 950 UV/Vis/NIR spectrometer in combination with an integrating sphere in order to collect also the scattered light. Analysis of the reflection and transmission data were carried out for the evaluation of the absorption coefficient α.

The absorption coefficient of thin films of 100 nm MoO_x / quartz with defined thickness, has been calculated using Eq. 4.1 at 25 °C:

$$\alpha = -\frac{1}{t} ln \left(\frac{\sqrt{(1-R)^4 + 4T^2R^2 - (1-R)^2}}{2TR^2} \right)$$

Eq.4.1

where α is the absorption coefficient, t is the thickness of the film, T and R are the transmission and reflectance, respectively [25]. The results were plotted as a function of energy of the incident photon energy in Fig. 4.3; since in the case of allowed direct transitions the absorption coefficien α can be expressed as

$$\alpha(hv) = A^*(hv - E_g)^{1/2}$$

Eq.4.2

, where A^* is a constant and E_g is the semiconductor band gap [26]. Thus, the band gap E_g can be calculated by extrapolation of the linear parts of the $\alpha^2 = f(hv)$ spectra to zero. The analysis of the absorption coefficient spectra revealed an E_g for MoO_x of approximately 3.8 eV, a value close to the reported data [8,27,28].

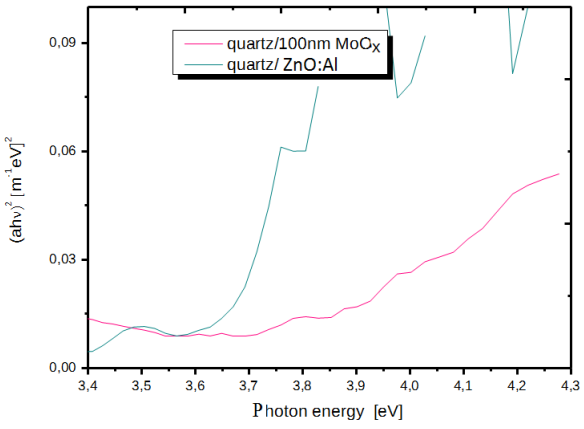

Figure 4.3 $(\alpha hv)^2$ vs. photon energy for ZnO:Al/quartz and 100 nm MoO_x/quartz.

4.3 Characterization at CISSY of the ZnPc:C_{60}/MoO_x interface

The chemical and electronic interface characterization of the physically deposited layers is studied by means of photoelectron spectroscopy. The theoretical background of photoelectron spectroscopy is further developed in chapter 3.

Because this technique is surface sensitive, to reach the ZnPc:C_{60} interface it is important to study samples with different thicknesses of the MoO_x layer, prepared as previously described.

The photoelectron spectroscopy characterization was carried out in the CISSY setup (CIS for $CuInS_2$ and SY for synchrotron). The experimental setup at the CISSY endstation consists of an analysis chamber containing the PES and the X-ray emission spectroscopy (XES) spectrometers, a central chamber for preparation procedures, which allows the simultaneous connection of preparation modules, a sample manipulator and a load-lock system for entry of the samples. The CISSY apparatus can be used alone, but a connection to the synchrotron is also possible. The set up is schematically presented in Fig. 4.4 and a view of the experimental setup is shown in Fig. 4.5.

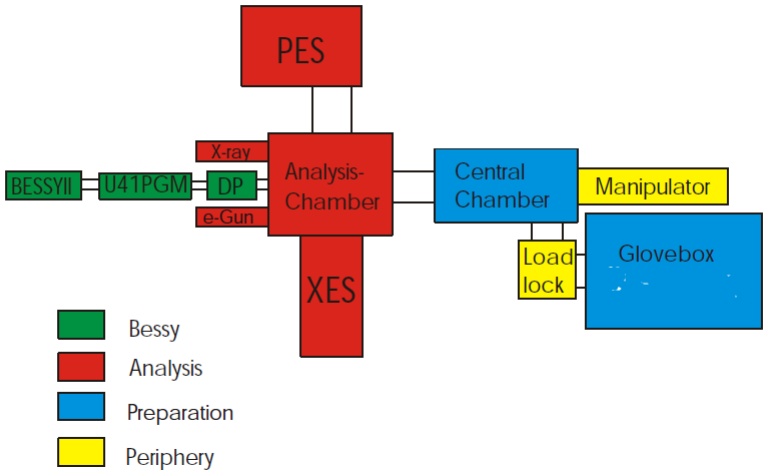

Figure 4.4 Schematic diagram of the CISSY experimental end station.

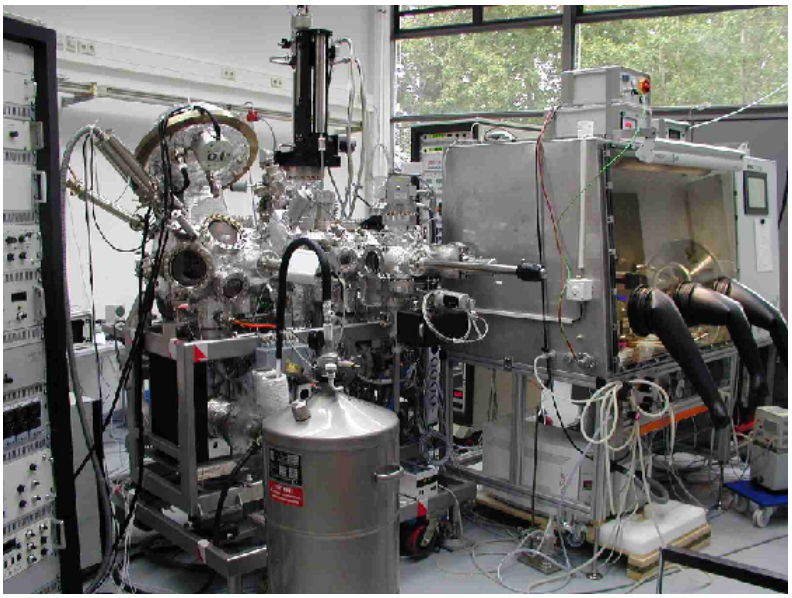

Figure 4.5 Photo of the CISSY experimental station were photoelectron spectroscopy measurements have been carried out.

Through the photoelectron spectroscopy electrons are emitted and detected by a detector, thus a start energy value and an end energy value must be specified to determine the energie interval that the detector must measure. Other parameters to be specified before the carrying-out of the photoelectron spectroscopy are the number of the scans and pass energy. During the analysis the number of the measured electrons is determined and shown as a spectrum.

After the measurements, the data are stored on the server and edited with the data analysis software IgorPro.

4.3.1 Ultraviolet photoelectron spectroscopy

The band alignment at the interface between active and buffer layer is an important aspect in thin film solar cells. The transport mechanism of the device depends on the energy band alignment and the work function values of the materials. Ultraviolet photoelectron spectroscopy (UPS) was used in this work to determine the workfunction values and, together with optical measurements, to determine the valence band offset.

The work function is the energy that an electron at the Fermi level requires to leave the matter, i.e. reach the vacuum level.

The work function was calculated by using the following formula:

$$\varphi = hv - E_k - E_f$$

Eq.4.3

where hv is the photon excitation energy, E_k the energy value at the secondary electron cutoff (SECO) and E_f the energy of the Fermi level [21].

The position of the secondary electron emission line was determined by linear extrapolation of the valence band spectrum at the high binding energy side. The intersection of the straight line with the x-axis corresponds to the kinetic energy. Substracting these and the energy of the Fermi level from the excitation energy of 21.22 eV the work function φ is determined.

The valence band edge was obtained from the linear extrapolation of the valence band spectra over the background level.

The valence band offset at the interface of ZnPc:C_{60} and MoO_x was estimated by combining the results of optical measurements, carried out with the Perkin-Elmer UV-VIS spectrometer, and the UPS analyses. For the determination of the Fermi level, a gold foil was used.

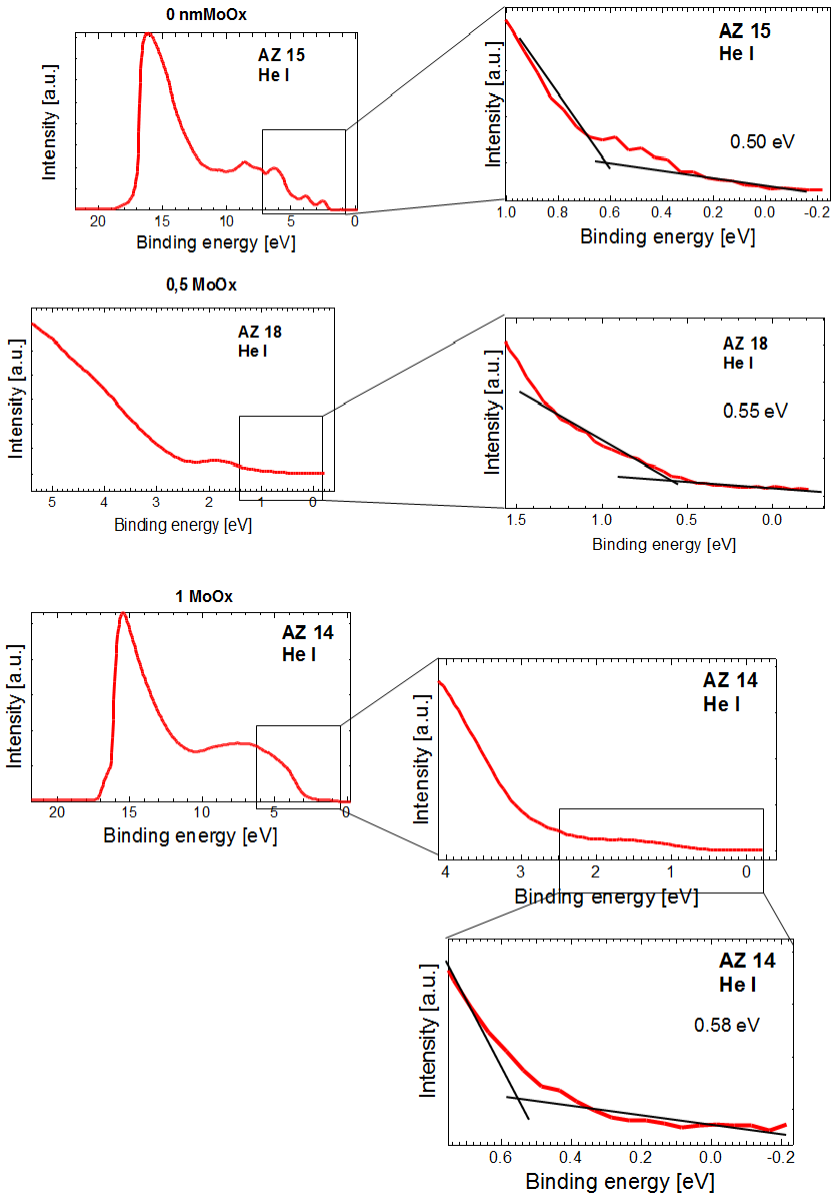

Figure 4.6 Ultraviolet photoelectron spectra for 0, 0.5 and 1 nm MoO_X showing the valence band maximum. The zero in the abscissa corresponds to the Fermi level which is obtained by measuring the Fermi edge of a gold foil with UPS. The spectra are recorded using the UV radiation source of He I ($h\nu$=21.22 eV). In the inset the difference between the Fermi level and the valence band values is shown.

4.3.2 X-ray photoelectron spectroscopy

XPS analyses were carried out with the aim of obtaining information about:

- Composition of the surface by identification of all elements (except H and He) present at concentrations > 0.1 atomic %;

- Oxidation state;

- Chemical shift: the binding energies of electrons in an atom are affected by the atom's chemical environment, thus shifts in photoemission peaks may indicate a change in the chemical environment of the element. This information is an useful tool to determine changes in the oxidation state of the surface. In this case, the binding energy increases due to the fact that part of the electronic density is transferred to the oxidizing species having higher electronegativity values. As a result, the electronic density of the oxidized substance becomes unbalanced against the positive nuclear charge;

- Auger signals: The reason for analyzing the Auger lines in photoemission spectrum is that the Auger electrons are more sensitive to chemical shifts than the respective photoelectrons.In the case of zinc compounds, the Zn photoemission lines may not show shifts in binding energy, whereas the corresponding Auger lines can shift several electron volts. In determining the chemical state of an atom, the evaluation of the so-called Auger parameter is a useful method. The Auger parameter is defined as the combination of the photoelectron binding energy and the kinetic energy of the related Auger electron. Many Auger parameters for known compounds are listed in the literature [29]. Since the energy difference between photoelectron and the related Auger electron of an element is fixed for a given chemical environment, any change in Auger parameters can be attributed to a change in the chemical environment of this element.

In determining the elements of the sample, the position of the photoemission peaks are compared with reference data available in the literature.

For the XPS analysis of the ZnPc:C_{60} and MoO_x interface a sample series consisting of samples with different MoO_x thickness was prepared by following the recipe explained in chapter 3.

The characterization of these samples gave a MoO_x thickness resolved information on the composition of the layers. After the preparation the samples are kept under N_2 environment to minimize contaminations from air.

All XPS analyses were all performed in ultra high vacuum conditions.

The characterization was performed using MgK_α and AlK_α X-ray sources.

A survey spectrum is taken as a start analysis.

The XPS survey spectra taken with AlK_{α} of the ZnPc:C_{60} and MoO_x interface are shown in fig. 4.7, for 0.5, 1, 2, and 5 nm thin film MoOx layers. The main peaks present are Zn2p, Mo3d, C1s, N1s, O1s, and Na1s.

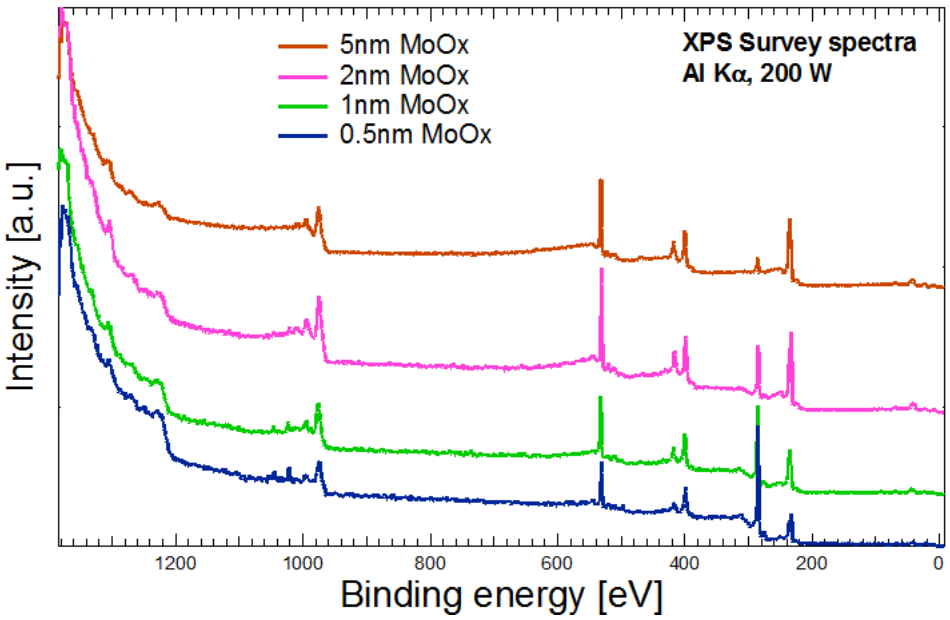

Figure 4.7 XPS survey spectra of the ZnPc:C_{60} and MoO_x interface for different MoO_x thicknesses.

The survey spectrum is a too coarse analysis for an accurate study of all the elements, thus for every single element new settings are needed.

The peaks positions data of the elements, presented in the table below, are taken from the literature database [29].

Table 4.1 Peaks positions of some spectral line of Zn, Mo, C, O and N [29].

Element	Spectral line	Binding energy [eV]
Zn	Zn2p	1021.4-1025.6
Mo	Mo3d	227.9-237.00
C	C1s	280.7-296.7
O	O1s	526.9-539.8
N	N1s	394.8-490.2

Detailed spectra of Zn2p signal and Zn_{LMM} Auger signals are shown in Fig. 4.8.

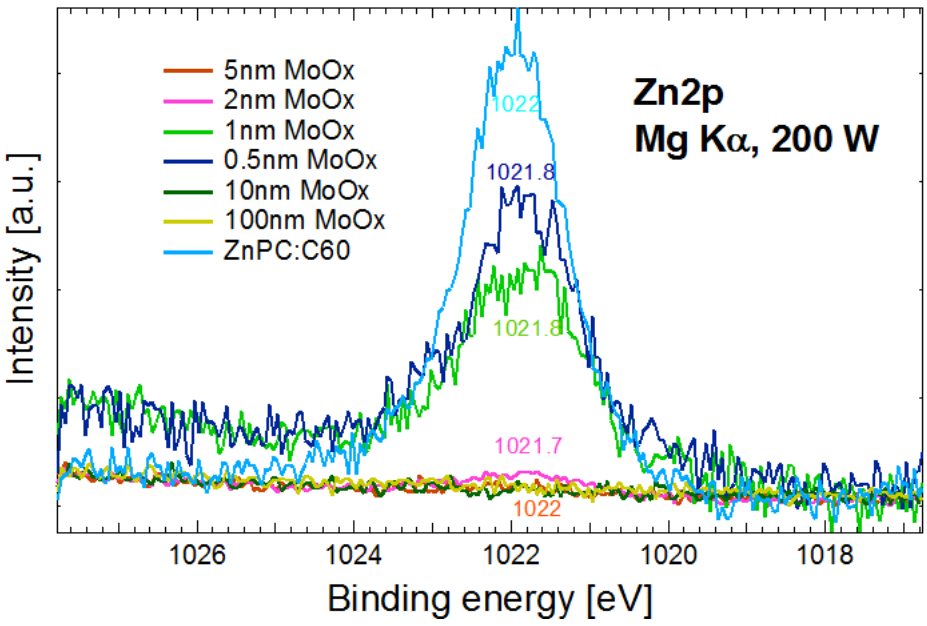

Figure 4.8 XPS spectra of the Zn2p signal for different MoO_x thicknesses. The energetic positions of the peaks are shown.

A decrease of the Zn2p peak signal with increasing thickness of the MoO_x layer can be observed. The peak signal is only lightly present for the 2 nm MoO_xsample and disappears for a thickness of 5 nm.

This means that the 2 nm thickness can be considered as the limit for a closed MoO_x deposited film on the organic layer.

The importance of the analysis of the zinc peak is related to the understanding of the morphology of the MoO_x layer. A compact oxide film is formed when no zinc peak is detected through the XPS analyses. Iin this case up to a oxide thickness of 2 nm the deposition of the MoO_x does not form a closed film, thus the zinc coming from the layer below is still detected. For thicker films the zinc peaks disappear, as it can be seen in Fig. 4.8, thus evidencing the compactness of the oxide layer, that covers completely the organic layer.

No evident shift in the Zn2p peak position was detected (Fig. 4.9).

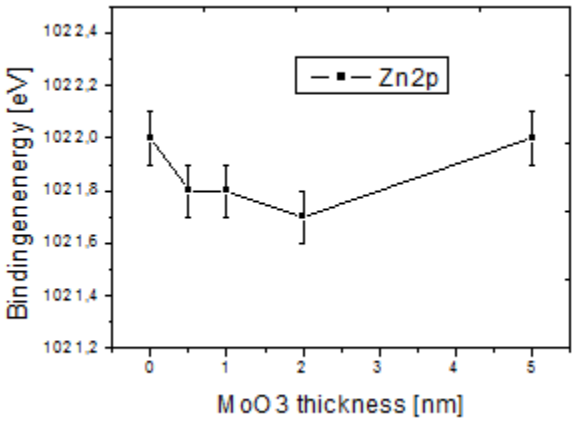

Figure 4.9 Zn2p peak position shift as function of the MoO_x thickness.

The Zn_{LMM} auger peaks are shown in Fig. 4.10. In order to assess the chemical environment of the Zn atom at different MoO_xthicknesses, the energy positions of the Zn_{LMM}peaks are compared with data extracted from literature [29].

The position of the Zn_{LMM} peaks suggest that in the sample without the MoO_x layer, the Zn is embedded in the organic layer, whereas in the sample with the MoO_x layer the Zn signal may come from Zn bound to oxygen atoms. The Auger kinetic energy values, presented in Table 4.2, show that the Zn signal, detected in the sample without the MoO_x, comes from an organic bond [29]. This means that the Zn detected in this layer is bound to organic molecules: in this case, the molecules of the ZnPc. In the samples with the MoO_x layer, on the other hand, the analysis of the Auger kinetic energy's values reveals a zinc-oxygen bond, that is, a zinc atom tied to oxygen atoms. All the Auger kinetic energy's values are taken from the Nist Database [29].

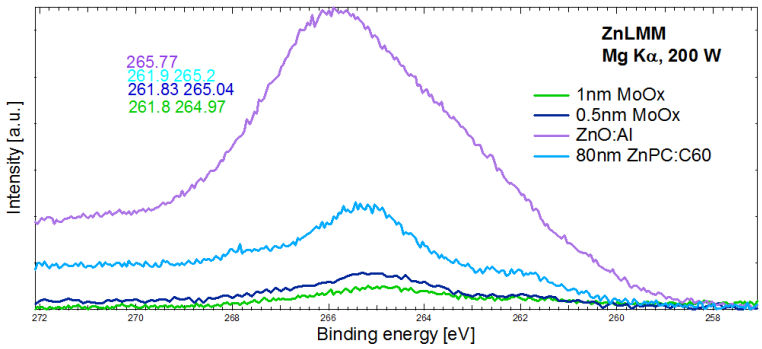

Figure 4.10 Zn_{LMM} Auger peaks spectra.

Table 4.2 Zn_{LMM} Auger peaks positions [29].

Element	Auger electron line	Auger kinetic energy [eV]	Formula
Zn	ZnLMM	987,7	Organic bound
Zn	ZnLMM	988	ZnO
Zn	ZnLMM	988,1	ZnO

For the analysis of the oxidation state of the buffer layer, the Mo3d peak signals for different MoO_x thicknesses are studied.

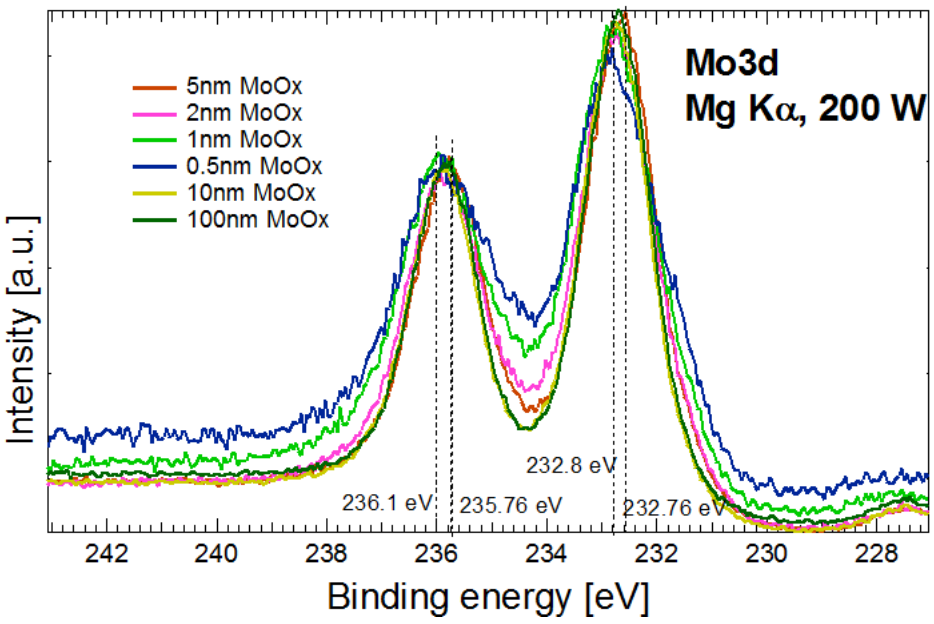

Figure 4.11 XPS MoO_X spectra of 0.5 to 10 nm of MoO_X buffer layer samples together with the reference sample of 100 nm MoO_X.

The energetic positions of the MoO_x peaks were compared with the data extracted from literature from the Nist Database [29]: MoO_3: 232.3 eV~233.1 eV; 235.8 eV~236.41 eV for different molybdenum oxides: the position of the peaks corresponds to that of MoO_3 in most of the literature data and some to MoO_2. Due to the fact that the literature data are taken from experimental measurements, the biggest probability is that the oxide present at the surface is a MoO_3.

Detailed peaks of the C1s, O1s and N1s signals are presented in Fig. 4.12.

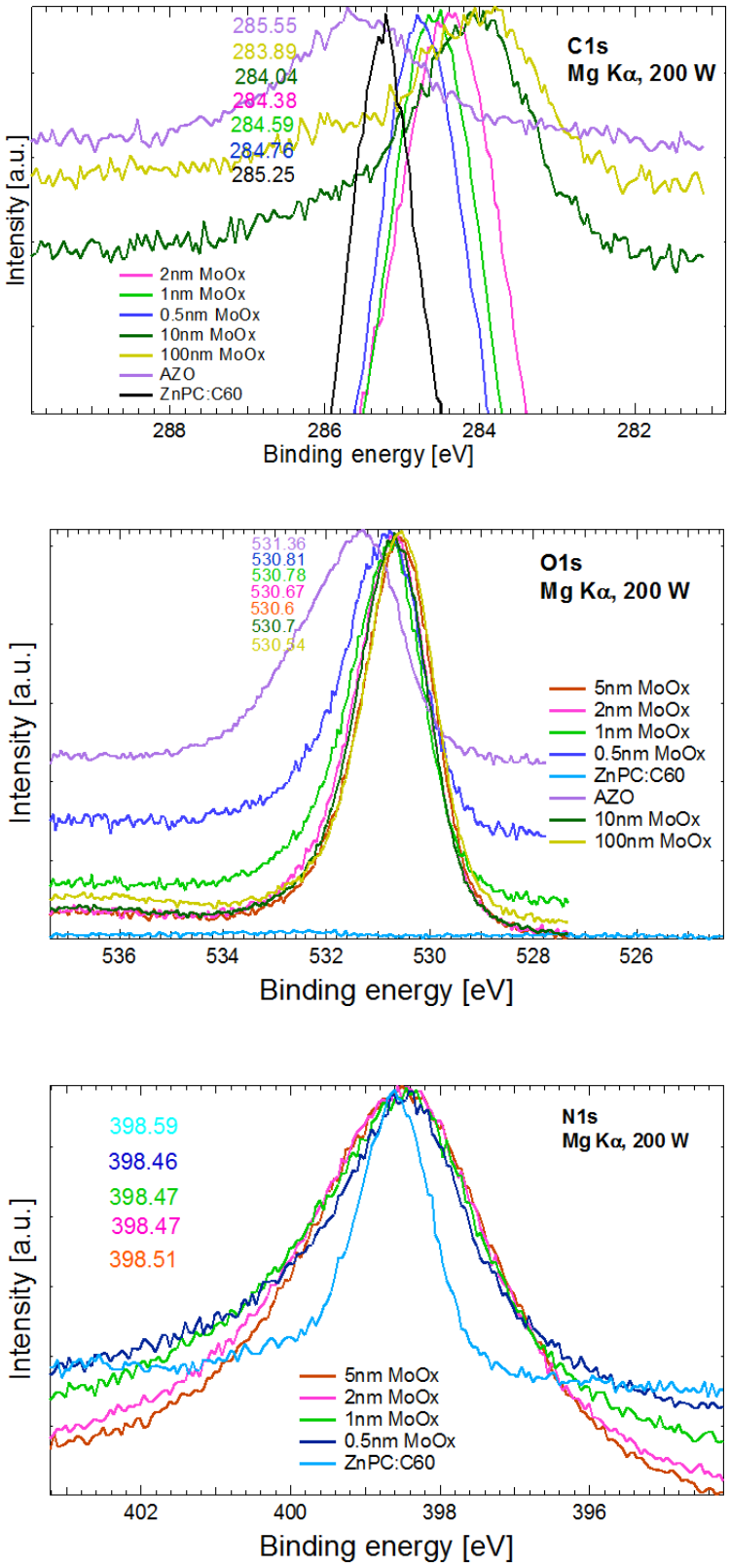

Figure 4.12 XPS detailed spectra of C1s, O1s and N1s peaks signals.

The carbon signal shown in Fig. 4.12 comes from the organic layer in the case of thin films up to 2 nm, where the thickness is still small enough to allow the detection of the carbon from the organic layer. In the case of thicker films the carbon signal comes from the carbon present as surface contamination, coming from the apparatus, and not anymore from the organic molecules. The peak signal in this last case is less evident than the thinner films. This explains the peak shift detected in the spectra of the carbon peaks. For intermediate thicknesses, the carbon signal is influenced both by the carbon of the organic bounds and that of the contamination: the thicker the MoO_x layer is, the bigger is the contamination influence.

The N1s photoemission peak comes from the organic molecules of ZnPc, which contains atoms of N (formula $ZnC_{32}H_{12}N_8$). The energetic position of the N1s peak with increasing thickness remains almost constant (Fig. 4.12), thus no chemical environment change takes place, but a change in the form of the peaks is to observe. In comparision with the sample without the MoO_xlayer, the other peaks have a bigger area. This correlated with the formation of new nitrogen bonds. Thus it can be expected that the molecules of ZnPc in contact with the phyisically deposited MoO_x change their type of bond.

The Mo3d peak area increases from 24.48 at room temperature to 30.17 at 200 °C

4.4 Temperature dependent J(V) measurements

The temperature dependent J-V measurements were performed on samples with an area of 0.2994 cm^2 inside a cryostat which has a transparent window allowing the light to pass through.

The aim of the thermal treatments is the study of the influence of the temperature on the ZnPc:C_{60}/MoO_x hybrid interface. In particular, the surface work function (WF) of the MoO_x thin films on ZnPc:C_{60} are here considered, as the WF parameter is a key step for the understanding and the possible optimisation of the electron properties of the hybrid interface.

The temperature range of the measurements was from room temperature up to 320°C with the following temperature steps: room temperature, 60°C, 80°C, 100°C, 120°C, 140°C, 160°C, 200°C, 240°C, 260°C, 280°C, 320°C. For each temperature the sample was annealed for 10 minutes.

To cool down the sample and ensure reaching of room temperature before each new temperature step, the sample was kept in contact with a cold conductive substrate for 5 min after each annealing step.

For switching from dark to illuminated measurement, a shutter on the transparent window is used. In order to record J(V) curves under different illumination intensities, a rotating wheel is

located between the halogen lamp and the shutter. The wheel has twelve different filters. One of them is totally transparent providing an illumination intensity of $I_{ilu} = 1$, approximately AM 1.5 [31].

The transparency of the filters decreases from the first to the last one. In this manner, at a given temperature, a J(V) curve is recorded first in the dark by closing the shutter, then the shutter is opened and J(V) curves are recorded under different illumination intensities, by means of the rotating filter wheel.

A direct relationship between short-circuit current density and the open-circuit voltage can be obtained by writing the equation 1.2 [10] at short-circuit condition ($J(V_{OC}) = 0$).

$$J_{SC} = J_0 \left[exp\left(\frac{qV_{OC}}{AkT}\right) - 1 \right] + \frac{V_{OC}}{R_P}$$

Eq.4.4

where the photogenerated current density is assumed to be the short circuit density. The current-voltage curves $J_{SC}(V_{OC})$ measured under different illumination intensities for a given temperature provide different points of the equation 4.4.

4.5 Temperature dependent photoelectron spectroscopy analysis

After carrying out of the J-V measurements as function of the substrate temperature, the ZnPc:C_{60}/MoO_x interface behaviour during the thermal treatments was investigated by UPS and XPS measurements. To allow a relation between the two analyses, the PES experiments were carried out with the same annealing conditions as the J-V measurements.

The sample analyzed in this investigation step had the same structure of the complete solar device characterized by J-V analysis. The ambient and temperature conditions were kept the same.

Annealing up to 320°C with the same temperature steps as the J-V analysis were reproduced in the photoelectron spectroscopy apparatus. A cooling of the sample after each annealing step was carried out to reproduce the same annealing procedure as for the J-V measurements.

A schematic graph of the annealing procedure is displayed in Fig. 4.13.

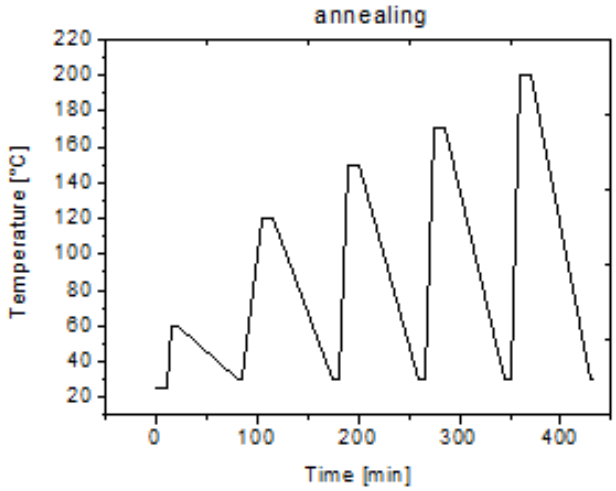

Figure 4.13 Graph of the annealing procedure.

The VB level was studied by analyzing the UPS spectra. Fig. 4.14 shows the UPS lines of the sample ZnO:Al/80 nm ZnPc:C_{60}/5 nm MoO_x in the VB range. In the graph are displayed also the spectra recorded during the thermal treatment.

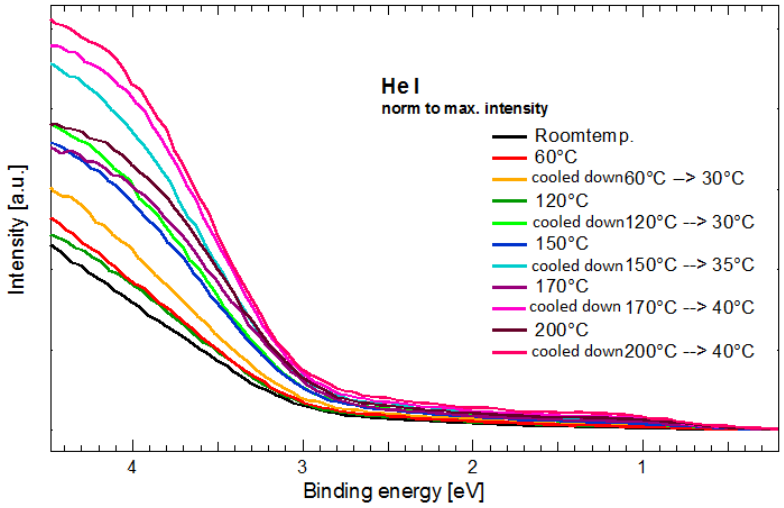

Figure 4.14 UPS spectra recorded during the annealing and after the cooling down for the sample ZnO:Al/ 80 nm ZnPc:C_{60}/ 5 nm MoO_x. Temperature values from room temperature to 200 °C are shown.

The VB position does not show any significant variation with the annealing temperature.

For the determination of the work function the UPS spectra in the region of the secondary emission line are considered. Fig. 4.15 shows the secondary emission lines for the annealed samples, where intermediate spectra recorded during the thermal treatments are also displayed.

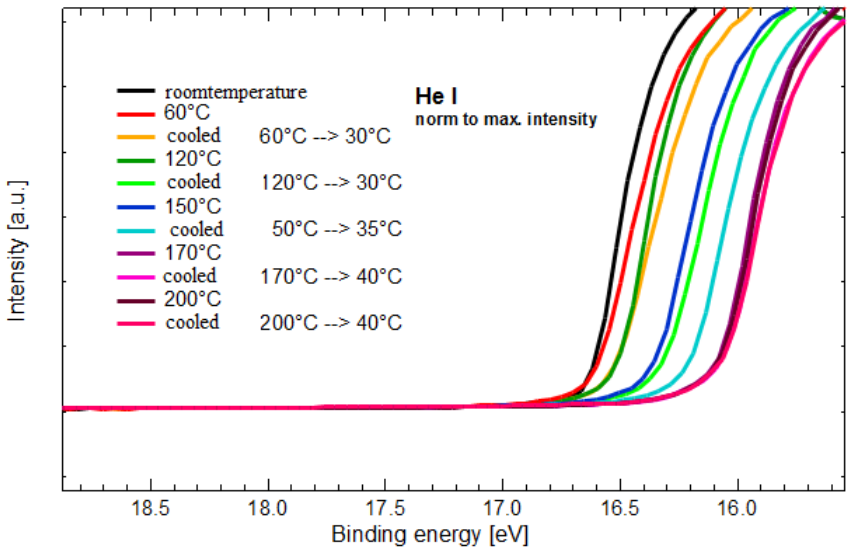

Figure 4.15 UPS spectra in the region of the secondary emission curve for different temperatures of the annealing process for the sample ZnO:Al/ 80 nm ZnPc:C_{60}/ 5 nm MoO_x. Shown are also the spectra recorded during the thermal process.

In Fig. 4.16 detailed spectra of the main photoemission peaks C1s, O1s, Na1s and Zn2p recorded by XPS for the ZnO:Al/ 80 nm ZnPc:C_{60}/ 5 nm MoO_x sample are shown.

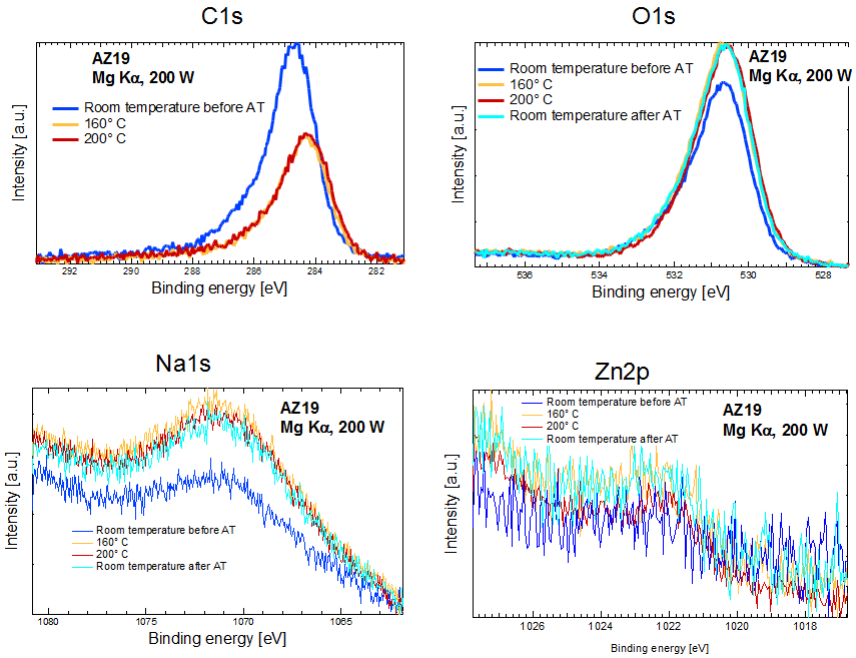

Figure 4.16 XPS detailed spectra of the C1s, O1s, Na1s and Zn2p photoemission peaks for a 5 nm MoO_3 sample at room temperature before the annealing procedure (blue), after the annealing procedure (light blue), annealed at 160°C (orange) and 200°C (red).

The carbon peak signals after annealing are of lower intensity.

This could be due to the evaporation of the carbon impurities present on the surface of the samples. Some carbon in form of oil in fact may be present at the cold sample surface. Due to the annealing procedure up to 200°C evaporation from the surface occurs, rendering the other elements signal peaks more visible to the detector. The carbon peak is the only one that through the annealing procedure decreases in intensity, while O1s, Na1s and, less evidently Zn2p, become more intense (Fig. 4.15).

The increase of Zn2p with the annealing can be related also to diffusion of the Zn in the direction of the MoO_x layer, evidencing the Zn2p peak signal.

Since the Zn2p energy position is the same as before the annealing, new Zn bonds can be excluded.

The increase of the Na1s signal could be related with a thermal diffusion of this element, as for the Zn2p. The Na source can be the glass substrate.

4.5.1 Peakfit

To allow a better evaluation of the normalized graphs and in order to estimate the ratio of the contributions of the different elements, the data are loaded in the Peakfit software [31] where the spectra are fitted with Voigt functions (the Voigt profile is a convolution of a Lorentz and a Gaussian profile), through which the background is eliminated. A base line is set and some extreme points of the graph are cut off. A suitable curve is placed under the peak. The area value and the peak coordinates are calculated by the Peakfit software. The full width at half maximum values of the photoemission signals of the peaks placed under the same line are kept constant during the fit and the resulting values are shown in table 4.3.

Table 4.3 Peaks area of the main photoemission peaks at room temperature and after thermal treatment of 200°C with their respective energetic positions.

Core level	Area RT	Area 200°C	P.Position RT	P. Position 200°C
Zn2p	0,0194	0,326 (0,0254+0,0070)	1022.8	1022 1023,7
O1s	4,2250	4,7304	530,78	530,67
C1s	3,3396	1,8314	284,79	284,39
Na1s	0,6980	0,7424	1070,7	1070,7
Mo3d	3,0534	3,7470	398,64	398,48
Mo3p	24,48	30,17	232,66 235,79	232,13 232,98 235,22 235,87

It can be observed in the table that the calculated area values of the photoemission peaks decrease with the annealing temperature for the carbon peak, while increasing for the other photoemission signals.

Energetic peak position do not show any considerable variations.

4.6 NEXAFS measurements

NEXAFS measurements were carried out at BESSY II, Berlin, Beamline SurICat, to monitor the influence of 1 nm MoO_x layer on the ZnPc:C_{60} organic surface.

Indicated in Fig. 4.17 are the Zn2p spectra for 1 nm MoO_x/80 nm ZnPc:C_{60}/ZnO:Al/Glass (blue line) and 80 nm ZnPc:C_{6060}/ZnO:Al/Glass (green line) samples.

NEXAFS spectra are usually measured either through the fluorescent yield, in which emitted photons are monitored, or total electron yield, in which the sample is connected to ground and the neutralization current is monitored.

Fluorescence (thick line) and sample current (thin line) analyses were carried out, fluorescence analysis has a deeper information sensitivity.

While the fluorescence curves in the two cases present almost the same trend, an evidently different signal is detected in the case of the sample current analysis, showing that a modification or interaction occurs in the first atom layers of the sample with the 1 nm MoO_x, thus evidencing how 1 nm MoO_x layer has an influence on the surface.

Further analyses would be required to allow for a complete NEXAFS characterization, these techniques need in fact many different reference analyses due to the lack of complete literature references.

The performed NEXAFS characterizations are the first step are the first stepof a promising direction of investigation for a detailed understanding of this interface.

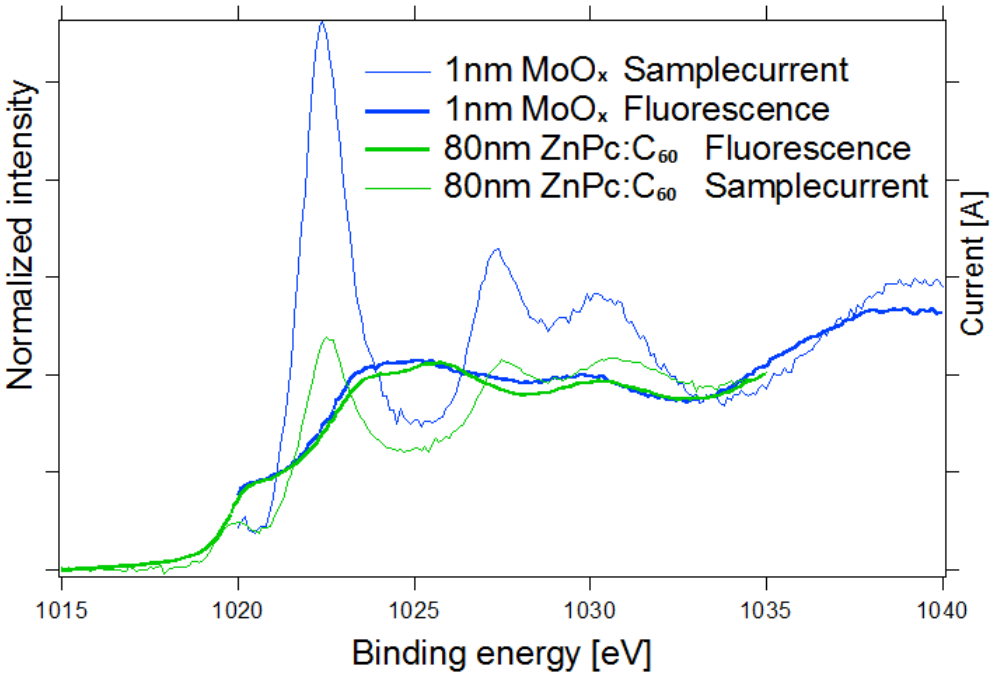

Figure 4.17 NEXAFS spectra of the Zn2*p* in the range 1015 eV-1040 eV for 1 nm MoOx/80 nm ZnPc:C_{60}/ZnO:Al/Glass and 80 nm ZnPc:C_{60}/ZnO:Al/Glass samples.

From the spectra shown in Fig. 4.17 informations about the influence of 1 nm MoO_x film presence on the organic surface are taken.

It is clearly visible in these spectra that the samplecurrent signals present a difference between the sample with and without the nanolayer of MoO_x. This indicates that even a very thin film of 1 nm MoO_x is able to induce a modification on the organic surface thus resulting in different peak's

signals. While a detailed comprehension of the peak's signals would require a further study, here it can be concluded that NEXAFS analyses are a succesfull method for the investigation of this hybrid interface, in particular the samplecurrent signals, because they are more surface sensible than the fluorescence signals. They in fact allow an investigation at a minor depth of the interface than the fluorescence studies.

5 Discussion and conclusions

5.1 Band alignment from UPS analysis

The work function results obtained with the UPS measurements are presented in Fig. 5.1.

The work function values derived from the UPS analysis for the MoO_3/ZnPc:C_{60} interface are (an error margin of 0.05 eV is considered): φ=4.12±0.05 eV for the reference sample without organic layer, φ=4,65±0.05 eV for the 0.5 nm MoO_3/ZnPc:C_{60} sample, φ=4,82 ±0.05 eV for the 1 nm MoO_3/ZnPc:C_{60} sample, φ=4,85 ±0.05 eV for the 2 nm MoO_3/ZnPc:C_{60} sample, φ=4,88 ±0.05 eV for the 5 nm MoO_3/ZnPc:C_{60} sample and φ=5.22 ±0.05 eV for the 10 nm MoO_3/ZnPc:C_{60} sample. The reference sample with 100 nm MoO_3 has a φ=5.30 ±0.05 eV. Measurements have been carried out at two different positions on the sample, to monitor the uniformity of the thin film.

The work function values were determined from the UPS spectra, from the position of the secondary electron emission line, as explained in the subsection 4.3.1.

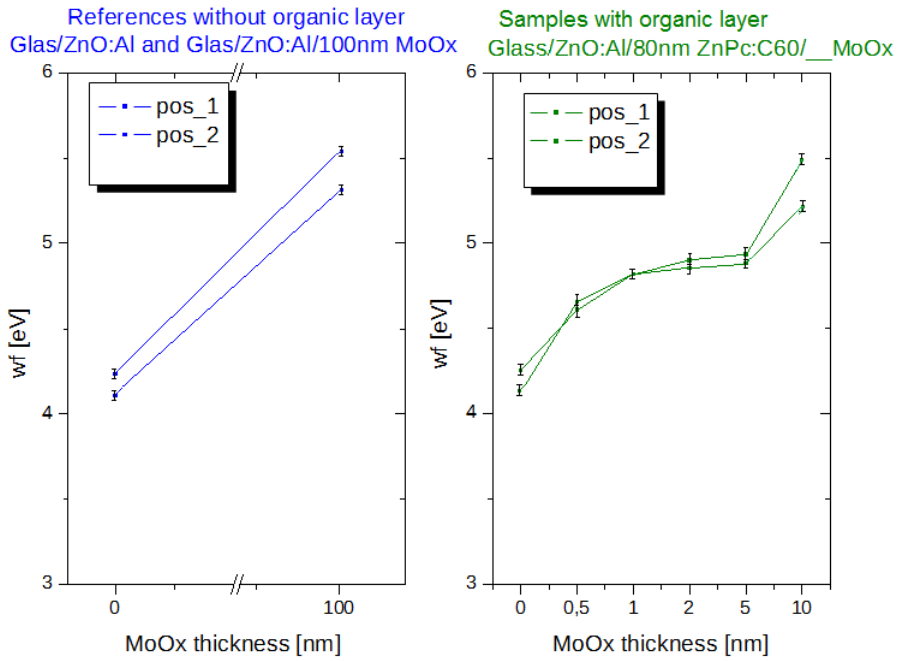

Figure 5.1 Work function values in function of the MoO_x thickness for two positions on the sample. The margin error of 0.05 eV is indicated.

Kelvin probe force microscope (KPFM) measurements from literature data, were taken into account to have a comparision with the UPS analysis carried out in this work. In table 4.3 data of

both the techniques are presented. KPFM is a scanning probe technique used to measure surface potentiometry (the difference in electrode potentials measurement) of a film. The KPFM operates in tapping mode, in a similar way to atomic force microscope (AFM), however, the tip-sample distance is increased. This separation makes the oscillations sensitive to long range electrostatic forces. The gradient of such forces is related to the potential difference between the tip of the microscope and the sample [4]. Unlike STM (scanning tunneling microscope), this technique measures an electrostatic interaction between two objects rather than a direct current flow [4]. As there is no contact between the tip and the sample it is a suitable technique for soft materials like conjugated polymers.

Table 5.1 Work function values obtained with KPFM and UPS analyses.

MoO_3-Thickness [nm]	WF-Dark KPFM [eV]	WF-UPS [eV]
0.5	5.093	4.7
1	5.195	4.8
3	5.245	4.9

The KPFM and the UPS workfunction results are in good agreement with each other, considering that KPFM and UPS requires different pretreatment: for KPFM preheating is needed to remove absorbed water, which changes the workfunction [32].

A pronounced work function increase with increasing MoO_3 thickness is observed up to a thickness value of 2 nm. Between 2 nm and 5 nm the workfunction value remains almost constant, while a marked jump between 5 nm and 10 nm is observed, which is taken as an error due to the experimental carrying out, probably due to a short exposing to air of one of the samples. From 5 nm to 10 nm the MoO_x layer should in fact behave as a bulk material and should not present differences.

The different work function's values in the interface region (up to 2 nm) could be related to the fact that the film of MoO_3 in that region is still not completely closed and compact, thus allowing a signal from Zn to be detected through the XPS analyses. In this case the work function calculated would be due to the presence both of the ZnPc and the MoO_3: the values are a result of a mixture of both the materials.

It has been frequently observed in previous works that a difference in the workfunction in an interface region is due to surface dipole moments [15]. The workfunction of a material depends on the electrical field that can be produced at the interface region by a surface dipole. As explained by

Koch et al in Ref. [15], in the absence of strong chemical interactions between the organic molecules and the oxide, the work function increases with the interface thickness by the "push-back" effect, where the oxide surface dipole is reduced by molecule adsorption due to Pauli-repulsion. Since MoO_3 and ZnPc:C_{60} exhibit rather weak interaction, it can be supposed that Pauli-repulsion and the associated charge redistribution may be an effect for the experimentally observed work function change at the interface.

A detailed understanding of this interface will although still require experimental investigations.

As already observed in the experimental chapter and shown in Fig.4.7 for the Zn2p photoemission peak, no appreciable energy shift in the XPS spectra has been observed with increasing MoO_3 thickness, signifying that no particular oxidation state change or interaction between the two materials takes places at the interface.

Together with the results of the optical measurements carried out for 100 nm MoO_3 samples, where an optical band gap for bulk MoO_3 of 3.8 eV was found, a theoretical transport mechanism of the device is presented in Fig. 5.2.

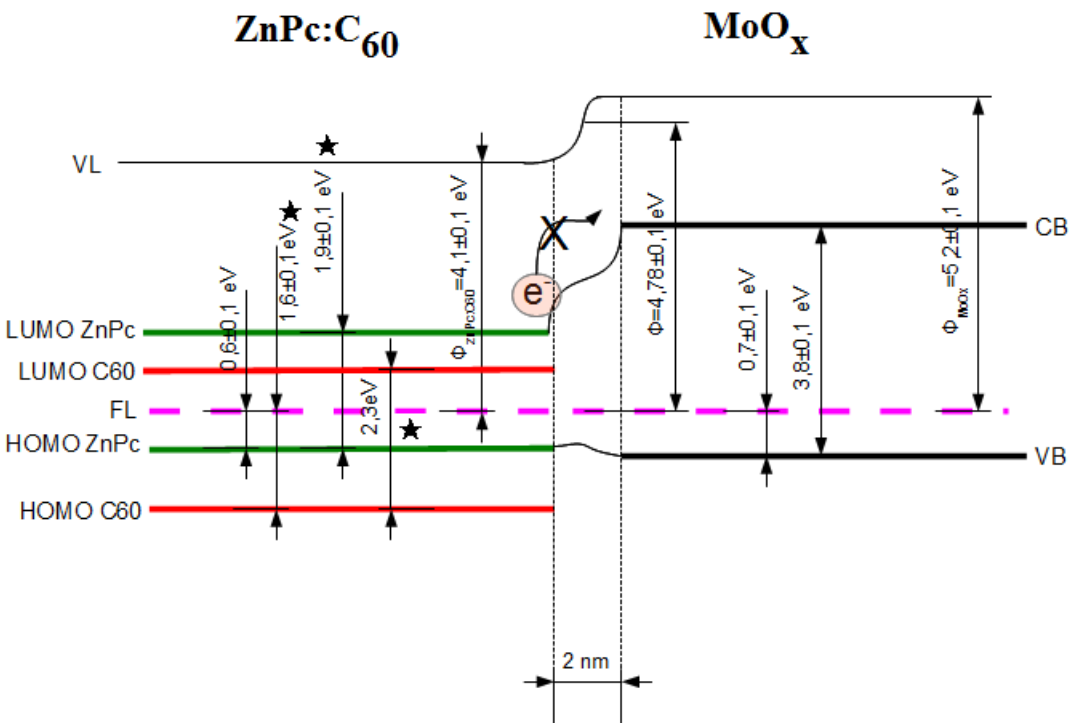

Figure 5.2 Schematic energy level diagram of the ZnPc:C_{60}/MoO_3 interface heterojunction. The experimentally determined band gap values of bulk MoO_x and the difference between valence band levels and Fermi levels as well as the literature data are given. [8,33].

This proposed energy diagram represents a successful mechanism for an hybrid interface, the CB level of the intermediate layer being higher than the LUMO of the donor (and even acceptor) material.

In this case, electrons produced in the photoactive layer and separated from the hole at the donor-acceptor interface, cannot jump in the wrong direction, as they would require an energy excitation to reach the CB of the buffer layer. The intermediate MoO_x layer acts in this proposed solar cell as a successfull electron blocking layer because it ensures an efficient charge transport in the solar cell, thus it contributes to an efficient functioning of the cell.

5.2 PV parameters

The PV parameters in dependance of the temperature are shown in Fig. 5.3.

It is visible in the graphs how an increase of all PV parameters takes place in two different steps: up to a temperature of 160°C first and with a minor slope up to 260°C. The further increase of the

temperature up to 260°C does not reduce the efficiency of the solar cell, but a decrease in the V_{OC} value can be observed.

The efficiency of the solar cell increases from 2.13 % (with no annealing procedure) up to 3.39 % (for an annealing temperature of 320°C).

The V_{OC} increases from 450 mV with no annealing procedure to 520 mV for an annealing temperature of 260°C.

The I_{SC} increases from $4.16 \cdot 10^{-3}$A to $4.88 \cdot 10^{-3}$A for the 320°C annealing temperature and the FF from 33.9 % to a maximum of 40.71 % for the 320°C annealing temperature.

It should be noted that the organic layer ZnPc:C_{60} has already been heated up to 150°C due to the OPVD deposition. However, this is not relevant since the main interest is the behaviour of the complete solar device, in particular of the interface organic/inorganic layers, is here the main interest.

A constant increase in the PV parameters between different temperature steps indicates the presence of a homogeneous thin film, which does not degrade during the annealing process.

The solar cells measured in this work were prepared on 06/08/2012 with the OPVD method described in section 4.1. The experimental data were compared with the as-prepared sample measurements carried out in 06/08/2012. Compared to this reference solar cell, stored for 160 days under N_2, without annealing process, the efficiency is improved more than 1%. The annealing processes were carried out in N_2 atmosphere.

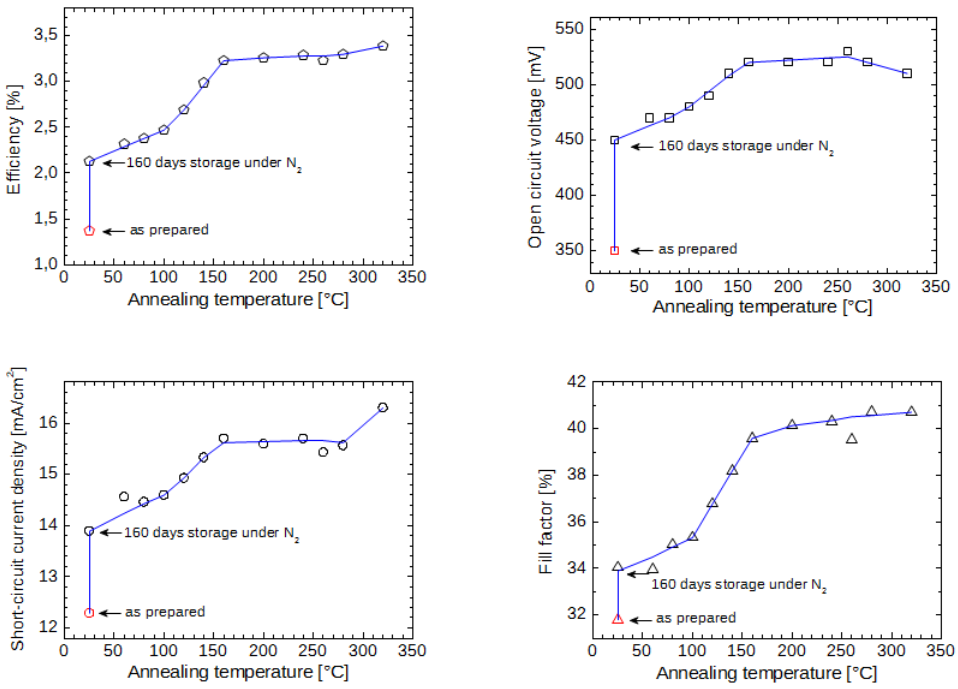

Figure 5.3 PV parameters as a function of temperature under AM 1.5 conditions (100mW/cm^2).

The parameters of the complete cell, shown in Fig. 5.4 and 5.5, were calculated from the J-V and the Log J-V curves.

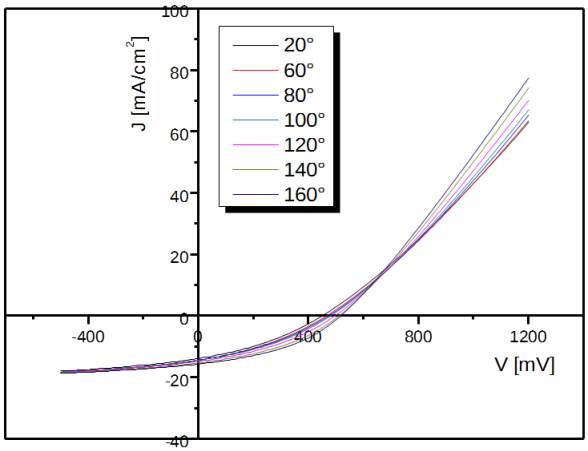

Figure 5.4 J-V curves of the annealed samples.

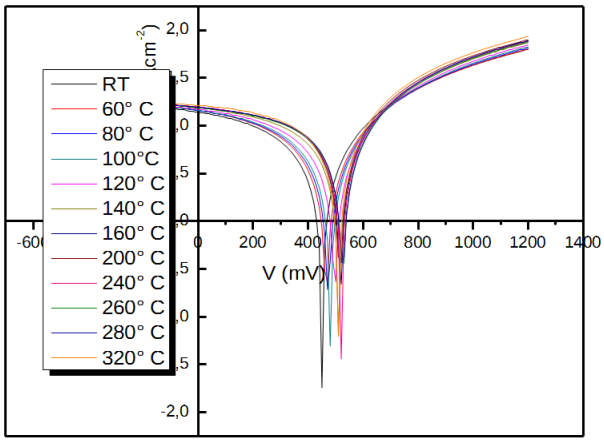

Figure 5.5 LogJ-V curves of the annealed samples.

The work function characterization in function of the annealing temperature is displayed in Fig. 5.6. The trend line is displayed (blue).

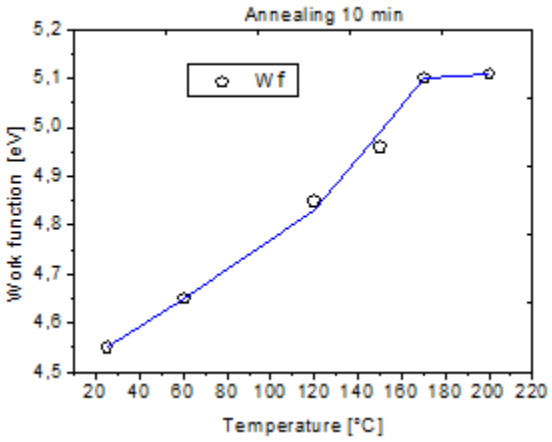

Figure 5.6 Wf values in function of the annealing temperature for the sample ZnO:Al/ 80 nm ZnPc:C_{60}/ 5 nm MoO_x.

A good correlation between the behavior of the device and the work function was found. The increasing of the work function at the interface with the temperature is correlated with the increase of the PV parameters.

This improvement of the solar cell behaviour with annealing treatments can be explained by means of optimisation of the bulk heterostructure. It has been already noticed by other authors [34,35] how annealing processes on polymer structures induce a nanomorphological arrangement of the donor and acceptor atoms, and often optimizes the percolated pathways, through which the separated charges transport in these blend layers occurs. The percolated pathways may in fact be interrupted due to the uncontrolled microscopic morphology, resulting in low efficiency devices. The reorganization of the structure may be the successful explication to increased efficiencies up to 3.39 %.

5.3 XPS annealing results

The temperature dependent photoelectron spectroscopy results carried out with the XPS are shown in Fig. 4.16.

The decrease of the carbon peak intensity due to the annealing is explained by means of evaporation process of the carbon oil present at the cold surface of the sample.

The increase of Zn2p and Na1s signals could be related with thermal diffusion of these element, furthermore, a reduction in thickness of any overlayer would also lead to an increase of the signals from the sample due to decreased electron absorption.

The Mo3d peak becomes bigger after the thermal treatment (Fig. 4.17). The Mo3d peak area increase may be due to the presence of more Mo atoms in the interface region. Formation of new types of chemical bonds can be excluded as from NIST database both the peaks energy positions indicate the same bond type, thus the increase could be explained with a diffusion process of the Mo with temperature.

A little shift in the energy position of the carbon peak is detected (0.4 eV), but it is considered to small to allow for a comparision with the literature data and an interpretation about the chemical environment. Data taken from literature [29] come in fact from experimental analysis, they are thus not sensitive enough to the 0.4 eV shift which is detected.

5.4 Concluding remarks

In this study, the interface structure and chemistry between the inorganic buffer layer of MoO_x and the organic photoactive layer of ZnPc:C_{60} in an organic solar cell with ZnO:Al as window layer has been engineered and investigated.

The aim of this experimental work was the control over the electronic structure of this semiconductor interface, in particular over the energy level alignment. As already mentioned in the introduction, charges have to be transported across this interface, and therefore low charge injection barriers are required. The mechanism governing the energy level alignment at this interface has been studied using XPS and UPS analyses.

A possible influence of the physically deposited MoO_x layer on the behavior of the adjacent ZnPc:C_{60} absorber was discussed using NEXAFS data.

Further experimental techniques, such as optical UV-VIS measurements and J/V analyses were used to better characterize the interface. A good charge carrier selectivity has been demonstrated from a buffer layer thickness of 2 nm, as shown in the energy diagram in Fig. 5.3.

Furthermore, the influence of the annealing temperature in such interface has been monitored by J/V measurements and PES and a good correlation between the Wf and the PV parameters measurements has been found: an optimisation of the ZnPc:C_{60}/MoO_x hybrid interface by an in-situ annealing in UHV has been obtained. The surface Wf of the MoO_x thin films on ZnPc:C_{60} were determined in the temperature range 25–200°C by UPS: a change from 4.57 eV to 5.20 eV was observed. In addition, annealing experiments in an N_2 atmosphere were performed on complete ZnO/ZnPc:C_{60}/MoO_x/Ag device structures in the temperature range 25–320°C and an significant improvement of the efficiency of complete devices has been observed. Three slopes has been observed

on PV paramenters curves. The observed slopes correlate well with the ones detected on the Wf graphs. Therefore it can be concluded that at the hybrid ZnPc:C_{60}/MoO_x interface thermally activated processes take place. The mechanisms of the thermal processes were correlated to interface chemistry.

References

[1] Arndt, Christoph. Information measures: information and its decription in science and engineering. Springer Verlag, 2001.

[2] Green, Martin A., et al. Solar cell efficiency tables (version 41). Progress in Photovoltaics: Research and Applications, 2013, 21.1: 1-11.

[3] Petty, Michael C. Molecular electronics: from principles to practice. Wiley-Interscience, 2008.

[4] Wright, Matthew; Uddin, Ashraf. Organic—inorganic hybrid solar cells: A comparative review. Solar Energy Materials and Solar Cells, 2012, 107: 87-111.

[5] http://heliatek.com, March 2013.

[6] http://blog.disorderedmatter.eu, March 2013.

[7] Krebs, Frederik C., ed. Polymeric solar cells: Materials, design, manufacture. Destech Publications Incorporated, 2010.

[8] Vogel, Mirko. Grenzflächen in Phthalocyanin-C60-Solarzellen. Diss. 2005.

[9] Persegona, Nicola. Le tecnologie fotovoltaiche. 2011.

[10] Petritsch, Klaus. Organic solar cell architectures.Cambridge and Graz 2000.

[11] Brabec, Christoph J., et al. Origin of the open circuit voltage of plastic solar cells. Advanced Functional Materials, 2001, 11.5: 374-380.

[12] Scharber, Markus C., et al. Design rules for donors in bulk-heterojunction solar cells—Towards 10% energy-conversion efficiency. Advanced Materials, 2006, 18.6: 789-794.

[13] Bundgaard, Eva; Krebs, Frederik C. Low band gap polymers for organic photovoltaics. Solar Energy Materials and Solar Cells, 2007, 91.11: 954-985.

[14] Sariciftci, N. S., et al. Photoinduced electron transfer from a conducting polymer to buckminsterfullerene. Science, 1992, 258.5087: 1474-1476.

[15] Blumstengel, Sylke, et al. Band-offset engineering in organic/inorganic semiconductor hybrid structures. Physical Chemistry Chemical Physics, 2010, 12.37: 11642-11646.

[16] Rusu, Marin, et al. Fine tailored interpenetrating donor–acceptor morphology by OVPD for organic solar cells. Thin Solid Films, 2008, 516.20: 7160-7166.

[17] Kröger, Michael, et al. P-type doping of organic wide band gap materials by transition metal oxides: A case-study on Molybdenum trioxide. Organic Electronics, 2009, 10.5: 932-938.

[18] Nicolaidis, Nicolas C., et al. Fullerene contribution to photocurrent generation in organic photovoltaic cells. The Journal of Physical Chemistry C, 2011, 115.15: 7801-7805.

[19] Li, G., et al. Efficient inverted polymer solar cells. Applied physics letters, 2006, 88.25: 253503-253503-3.

[20] Briggs, David; Seah, Martin P. Practical surface analysis by Auger and X-ray photoelectron spectroscopy. D. Briggs, & M. P. Seah, (Editors), John Wiley & Sons, Chichester 1983, xiv+ 533, 1983.

[21] Risch, Lisa. Untersuchung der ZnO:Al/CuInSe2-Grenzfläche mithilfe von Photoelektronenspektroskopie. Masterarbeit, 2012.

[22] Rusu, Marin, et al. Organic donor, acceptor and buffer layers of small molecules prepared by OVPD technique for photovoltaics. Renewable Energy, 2008, 33.2: 254-258.

[23] Forrest SR. Nature 2004;428:911.

[24] M. Heuken, N.Meyer, in: H. Klauk (Ed.), Organic Electronics,Wiley-VCH, Weinheim, 2006, ISBN-10: 3-527-31264-1, ISNB-13: 978-3-527-31264-1.

[25] Rusu, Marin, et al. Solar cells based on CCSVT-grown CuGaSe2—absorber and device properties. Thin solid films, 2005, 480: 341-346.

[26] J.I. Pankove, Optical Processes in Semiconductors, Dover, New York, 1976, p. 36.

[27] Brown, Patrick R., et al. Improved Current Extraction from ZnO/PbS Quantum Dot Heterojunction Photovoltaics Using a MoO3 Interfacial Layer. Nano letters, 2011, 11.7: 2955-2961.

[28] Zhang, F. J., et al. Inverted small molecule organic solar cells with Ca modified ITO as cathode and MoO< sub> 3</sub> modified Ag as anode. Solar Energy Materials and Solar Cells, 2010, 94.12: 2416-2421.

[29] http://srdata.nist.gov/xps, December 2012.

[30] Ümsür, Bünyamin. Electronic characteristics and transport mechanisms at chemical bath deposited-Zn(S,O)/Cu(In,Ga)(S,Se)2 heterojunctions. Master Thesis, October 2012.

[31] Peakfit software version 4.12 SeaSolve Software Inc., 1999-2003.

[32] Johnev, Boyan. Chemical engineering of the electronic properties of ITO-organics interface in Phthalocyanine/C60-Fullerene organic solar cells. 2006. PhD Thesis.

[33] Kessler, B. Phthalocyanine-C60 composites as improved photoreceptor materials?. Applied Physics A: Materials Science & Processing, 1998, 67.2: 125-133.

[34] H. Hoppe, M. Niggemann, C. Winder, J. Kraut, R. Hiesgen, A. Hinsch, D. Meissner, N.S. Sariciftci, Adv. Funct. Mater. 14 (2004) 1005.

[35] L.H. Nguyen, H. Hoppe, T. Erb, S. Günes, G. Gobsch, N.S. Sariciftci, Adv. Funct. Mater. 17 (2007) 1071.

[36] Chu, Chih-Wei, et al. High-performance organic thin-film transistors with metal oxide/metal bilayer electrode. Applied Physics Letters, 2005, 87.19: 193508-193508-3.

[37] Meyer, Jens, et al. Effect of contamination on the electronic structure and hole-injection properties of MoO/organic semiconductor interfaces. Applied Physics Letters, 2010, 96: 133308.

[38] Kyaw, A. K. K., et al. An inverted organic solar cell employing a sol-gel derived ZnO electron selective layer and thermal evaporated MoO_3 hole selective layer. Applied Physics Letters, 2008, 93.22: 221107-221107-3.

[39] Hofmann, Albert. The physics of synchrotron radiation. Cambridge University Press, 2004.

[40] Wiedemann, Helmut. Synchrotron radiation. Springer Verlag, 2003.

[41] http://helmholtz-berlin.de, March 2013.